Lawrence Berkeley National Laboratory

Esimation of field-scale thermal conductivities of unsaturated rocks from in-situ temperature data

Authors
Mukhopadhyay, Sumit
Tsang, Yvonne W.
Birkholzer, Jens T.

Publication Date
2008-04-28

Peer reviewed

Estimation of Field-Scale Thermal Conductivities of Unsaturated Rocks From In-Situ Temperature Data

Sumit Mukhopadhyay*, Yvonne W. Tsang, and Jens T. Birkholzer

Abstract

A general approach is presented here which allows estimation of field-scale thermal properties of unsaturated rock using temperature data collected from *in situ* heater tests. The approach developed here is used to determine the thermal conductivities of the unsaturated host rock of the Drift Scale Test (DST) at Yucca Mountain, Nevada. The DST was designed to obtain thermal, hydrological, mechanical, and chemical (THMC) data in the unsaturated fractured rock of Yucca Mountain. Sophisticated numerical models have been developed to analyze these THMC data. However, though the objective of those models was to analyze "field-scale"(of the order of tens-of-meters) THMC data, thermal conductivities measured from "laboratory-scale" core samples have been used as input parameters. While, in the absence of a better alternative, using laboratory-scale thermal conductivity values in field-scale models can be justified, such applications introduce uncertainties in the outcome of the models. The temperature data collected from the DST provides a unique opportunity to resolve some of these uncertainties. These temperature data can be used to estimate the thermal conductivity of the DST host rock and, given the large volume of rock affected by heating at the DST, such an estimate will be a more reliable effective thermal conductivity value for field-scale application. In this paper, thus, temperature data from the DST are used to develop an estimate of the field-scale thermal conductivity values of the unsaturated host rock of the DST. An analytical solution is developed for the temperature rise in the host rock of the DST; and using a nonlinear fitting routine, a best-fit estimate of field-scale thermal conductivity for the DST host rock is obtained. Temperature data from the DST show evidence of two distinct thermal regimes: a zone below boiling (wet) and a zone above boiling (dry). Estimates of thermal conductivity for both the wet and dry zones are obtained in this paper. Sensitivity of these estimates to the input heating power of the DST is also investigated in this paper. These estimated thermal conductivity values are compared with core measurements and those estimated from geostatistical simulations.

Note that the approach presented here is applicable to other host rock and heater test settings, provided suitable modifications are made in the analytical solution to account for differences in test geometry.

Sumit Mukhopadhyay, Yvonne W. Tsang, and Jens T. Birkholzer, Ernest Orlando Lawrence Berkeley National Laboratory, Earth Sciences Division, One Cyclotron Road, Berkeley, CA 94720.

* Corresponding author (SMukhopadhyay@lbl.gov)

1. Introduction

The Drift Scale Test (DST), located in the Topopah Spring middle nonlithophysal (Tptpmn) stratigraphic unit of Yucca Mountain, Nevada, is the largest *in situ* heater test ever conducted in fractured welded tuff. The DST was designed to investigate the coupled thermal-hydrological-mechanical-chemical (THMC) changes in the host rock caused by long-term heating. Data collected from the DST are assisting scientists and engineers to develop an understanding of the THMC changes likely to be encountered in the host rock around the high-level radioactive waste repository at Yucca Mountain. A more detailed discussion about the DST and analyses of the thermal-hydrological (TH) changes arising out of the DST can be found elsewhere [*Birkholzer and Tsang,* 2000; *Mukhopadhyay and Tsang,* 2003; *Birkholzer et al*., 2005].

After initiating the DST on December 3, 1997, heating was continuously provided by electrical heaters for slightly more than four years. During this heating phase, a substantial volume of rock experienced a significant increase in temperature, along with associated THMC changes. An extensive active and passive data collection system allowed monitoring of these THMC changes in the rock. The objective of this paper is to utilize the temperature data from the DST for estimating, *in situ*, thermal conductivities of the DST host rock. Given the large volume of rock heated during the DST, it is reasonable to expect that thermal conductivities estimated in such a manner would reflect appropriately the field-scale thermal conductivities of the DST host rock. This affords a unique opportunity to assess how field-scale thermal conductivities correlate with those derived from laboratory measurements. Using the field-scale thermal conductivities, instead of those from core measurements, would also help to reduce uncertainty in the prediction of long-term THMC conditions in the vicinity of the repository (a critical factor affecting repository performance).

Estimating the thermal conductivities of unsaturated rock from measured temperature data becomes non-trivial because of water saturation changes during the heating process. The fractured welded tuff surrounding the DST has a matrix water saturation of approximately 85-90% [*Tsang et al*., 1999; *Bechtel SAIC Company*, *BSC*, 2004] prior to commencement of heating. Hence the rock can be considered "wet" under ambient conditions. During the early phases of heating in the DST, heat transfer occurred entirely through this wet rock. With continued heating, as the temperature approached boiling near the heat source, the water in the matrix pores was converted to vapor, which then moved away from the source of heating and condensed in the cooler parts of the rock. The condensate thereafter flowed through the network of fractures either under gravity drainage or was absorbed in the rock matrix because of stronger capillary forces in the latter. Such simultaneous flow of vapor and condensate gave rise to what could be called "heat-pipe" signatures, a flat zone (at the boiling temperature) in a temperature vs. time or distance plot. The temperature data collected from the DST showed pervasive evidence of these heat-pipe signatures [*Birkholzer and Tsang*, 2000; *Mukhopadhyay and Tsang*, 2003; *Birkholzer*, 2006a]. With continued heating and boiling of pore water, a "dryout" zone formed in the host rock in the vicinity of the heat source, and rock temperature exceeded boiling point of water in the dryout zone. Outside of the dryout zone, the rock continued to be "wet," with temperatures below the boiling point of water.

Thus, the temperature data of the DST are indicative of heat transfer occurring in three distinct regimes. In the vicinity of the heat source (particularly, in the dryout zone), heat transfer occurs through the superheated dry rock. At the same time, far away from the heat sources, heat transfer takes place through the wet rock (see discussion below on measured saturation data from the DST). In both of these regimes, the primary mechanism of heat transfer is conduction. In between these two regimes is the two-phase 'transition' regime, where most of the boiling occurs, and where heat transfer is by means of both conduction and convection [*Birkholzer*, 2006a,b]. We shall discuss the DST temperature data in terms of these three regimes. Although the transformation from the wet- to the dry- rock scenario is dynamic and continuous, we present in this paper an analysis of the temperature data that enables estimation of the wet and dry thermal conductivities of the rock. The ability to arrive at the field-scale wet and dry thermal conductivities from actual temperature changes in the rock is important since the host rock, after emplacement of radioactive wastes, is expected to experience similar "wet" and "dry" conditions

It needs to be emphasized here that temperature rise in the host rock of the DST is a result of coupled thermal and hydrological processes including heat conduction through the rock, fluid migration (movement of water and vapor as described above) including convective transfer of heat, phase changes, radiative heat transport, and natural convection. Since the porosity of the DST host rock is only about 10-15%, mass of the solid rock is relatively large in any given volume compared to the mass of the fluids involved. As a result, among the different heat transfer mechanisms, heat conduction is the dominant contributor in transporting heat in the DST host rock (because a majority of the rock mass is solid), and is essentially controlled by the thermal conductivity (k) and thermal diffusivity (α) of the rock. State of the art numerical models have been developed to analyze the temperature data from the DST [*Birkholzer and Tsang*, 2000; *Civilian Radioactive Waste Management Systems*, *CRWMS*, 2000; *Mukhopadhyay and Tsang*, 2003; *Birkholzer et al.*, 2005]. For these numerical models, representative values of k and α of the host rock are provided as input. These input parameters are derived from laboratory measurements of thermal properties of cores collected from various boreholes in or around the DST test block [*Brodsky et al.*, 1997]. Here we adopt an approach to determine the thermal properties of the DST host rock using the temperature data from the DST. Since such an estimation (based on actual measured temperature data) is expected to represent the field-scale thermal conductivity, it will afford us the opportunity to compare the laboratory-scale measurements with the field-scale estimates. It will also let us decide whether the laboratory-scale measurements are appropriate input parameters for the THMC models or not.

Estimating thermal conductivity of solids from temperature data when heat conduction is the sole transport process is common practice [*Carslaw and Jaeger*, 1959]. More specifically, estimation of thermal properties of rock from inversion of measured temperature data has also been reported [e.g., *Gehlin*, 1998; *Lehmann et al*., 1998; *Kolditz and Clauser*, 1998; *Vosteen et al*., 2003]. However, estimating thermal properties of unsaturated, porous rock (as in the DST) from temperature data is challenging because of the coupling of TH processes. As a result, determination of thermal conductivity in this instance is an exercise not only of analyzing heat conduction but also of fluid flow processes. Furthermore, in principle at least, the thermal properties of the host rock may be derived from the DST temperature response by an inverse modeling approach, using software such as the ITOUGH2 [*Finsterle*, 1999], which accounts for the coupled TH processes while calibrating properties to measured data. For example, ITOUGH2 [*Finsterle*, 1999] has been successfully used [*Engelhardt et al*., 2003] to obtain hydrological (permeability and capillary strength parameters) and thermal (conductivity and specific heat) properties of mixtures of sodium bentonite and crushed rock by joint inversion of measured laboratory-scale pressure, drained-water volumes, and temperature data. Such an ITOUGH2-based inverse modeling involves many forward simulations of the TH processes associated with heating unsaturated porous rock. In practice, however, the inverse approach is less than optimum for large-scale heater tests such as the DST, since given the complex geometry of the DST and the complexities of the physical processes, a single forward three-dimensional TH simulation of the DST itself requires close to four weeks' computation time on some of the fastest machines currently available.

We have instead adopted an alternative efficient methodology to obtain reliable field-scale estimates of thermal conductivities. This alternative approach is based on an analytical solution for the spatial and temporal evolution of temperature rise caused by heating at the DST, assuming that the rock is homogeneous and isotropic. The assumption of homogeneity implies that the small-scale variabilities in thermal conductivity have been averaged over in the estimated field-scale value. The assumption of isotropy is justified as thermal conductivity data from core samples [*Brodsky et al*., 1997] do not provide sufficient evidence to the contrary. Finally, it is also assumed that the thermal properties are independent of temperature. In other words, the estimates of the thermal conductivities from the model should be construed as averaged over the appropriate temperature range. Also, the estimated thermal conductivities represent values over appropriate saturation ranges. Finally, it is also assumed that contribution of convective heat transfer is negligible outside the transition zone (i.e. outside the two-phase zone), a further discussion on which can be found in *Birkholzer* [2006a,b].

We first develop an analytical solution for temperature rise in the rock owing to the heat delivered by the heaters in the DST. However, since substantive boiling takes place in the DST rock and some of the resultant vapor leaves the DST domain through an open bulkhead (see Section 2), not the entire power output of the heaters goes to raising rock temperatures (i.e., some heat is lost). We account for this by following the boiling isotherm in the measured temperature data, and calculating the power that goes into heating and boiling of pore water. To reduce uncertainty in the estimated power that goes into heating and boiling of water, we also utilize results from numerical models for the DST [*Birkholzer and Tsang*, 2000; *Mukhopadhyay and Tsang*, 2003; *Birkholzer et al*., 2005]. The difference of total heater power output and the power utilized for heating and boiling of water gives the power used in heating the rock. With this latter power as input to the analytical solution, and comparing the analytical solution with the measured temperature rise at any given location and at any given time, we obtain the thermal conductivities using a nonlinear parameter estimation technique based on Gauss-Newton approach. In practice, our approach is quite general and can be used for estimating thermal properties of unsaturated rock from any heater test data, provided modifications are made to the analytical solution to account for the geometry of the test.

As stated earlier, the matrix pores of the DST host rock is about 85-90% [*Tsang et al*., 1999; *BSC*, 2004] saturated with water under ambient conditions. Measured temperature and saturation data from the DST show that saturation does not change significantly with continuous heating until temperatures approach boiling [*BSC*, 2004]. Thereafter, within a very narrow band around the boiling temperature, saturations decline sharply as boiling takes place and the rock becomes dry. Once the boiling front passes, some residual water remains in the rock, though the residual saturation is minimal compared to the ambient saturation [*BSC*, 2004]. Since saturation drop with temperature rise occurs along virtually a sharp front, DST temperature data can be analyzed separately for two temperature (or saturation) ranges. The first, where the temperatures are below boiling, the estimated thermal conductivity represents the thermal conductivity of the wet (nearly fully saturated) rock. On the other hand, thermal conductivity estimated from above boiling temperatures represents dry thermal conductivity of the rock because of the creation of virtually dry conditions above boiling. More discussion on this is provided later in the paper.

The rest of the paper is organized as follows. We begin with a brief description of the DST. Then we present some representative temperature and saturation data collected from the DST, and illustrate the various thermal regimes encountered in the DST during heating. Thereafter, we provide the analytical solution for spatial and temporal evolution of temperature rise in the host rock surrounding the host rock. We also discuss the nonlinear fitting techniques used in this section. In the section after that, we analyze the results from four numerical simulation experiments to determine the uncertainty in the thermal properties that are estimated using our proposed approach. Next, we present a methodology to calculate the power utilized in heating rock. The findings from our analyses of the DST temperature data are presented thereafter. Providing a summary of methods and results concludes the paper.

2. Description of the DST

The DST consists of a 47.5 m long, 5 m diameter Heated Drift (HD). A bulkhead separates the heated section from the unheated section of the drift; it also serves as the origin of the coordinate system in our calculations. The bulkhead is not completely impermeable, therefore some vapor generated within the rock may have escaped through the bulkhead during the test, accounting for some heat loss. Heating in the DST started on December 3, 1997, and ended on January 14, 2002. Heat was provided by 9 canister (or floor) heaters placed along the floor of the HD. Heating was also supplied by 50 rod heaters, each installed in 11-m-long borehole drilled orthogonal to the axis of the HD.

There are 25 rod heaters (hereafter referred to as wing heaters) on each side of the HD. Each of the wing heaters is composed of two 4.44-m-long sections: the inner (closest to the HD) wing heater and the outer wing heater. The inner wing heater starts at 1.67 m from the HD. There is a gap of 0.66 m between the inner and outer wing heater. Temperature data from the DST were continuously monitored by approximately 1,700 resistance temperature devices (RTD) placed in 26 boreholes. Each of these 26 boreholes is collared at the wall of the HD and is approximately 20 m in length. They form radial arrays (Boreholes 133–134, 137–144, 158–165, 168-169, 170–175) in five planes perpendicular to the HD, orienting either vertically, horizontally, or at an angle of 45^o with the HD. Figure 1 shows a schematic picture of the HD, the bulkhead, the wing heaters, and the locations of the temperature data collection boreholes. A more detailed description of the DST and the data collection boreholes can be found in *CRWMS* [1998].

In addition to the radial arrays of the temperature measurement boreholes, Figure 1 also shows two other horizontal boreholes (Boreholes 79 and 80), parallel to the axis of the HD. Each approximately 60 m long, they are located at about a distance of 9.5 m from the center of the HD and on either side (left and right) of it. They are also situated above the wing heaters, at about an elevation of 3 m above the center of the HD, with Borehole 79 being closer to the wing heaters by approximately 0.5 m compared to Borehole 80 (Borehole 79 dipped towards the end). These two boreholes are used both for temperature measurements and neutron logging (which is used to determine moisture content in the DST host rock). While we present saturation measurements only from the neutron logs in this paper, ground penetrating radar (GPR) surveys and electrical resistance tomography (ERT) were also conducted at the DST to determine changes in rock water content with heating.

The total design power of the nine canister heaters was 67 kW; and that of the 50 wing heaters was 143 kW [*CRWMS*, 1998]. The actual heat output from these heaters varied somewhat during the course of the test (which included a few power outages). Figure 2 shows the actual total heat output from these heaters as a function of time. Starting at 27 months of heating (March 2000), power was intentionally reduced, in a series of steps, to keep the temperature at the wall of the HD at a targeted maximum of 200^{o}C. In the analysis that follows, we will use an average over a certain time (0–6 months, 0–12 months, etc.) of the actual heat output from the heaters as the total power available for heating during that time period. Table 1 shows the calculated average of the actual heating power at different times during heating.

3. Measured Temperature and Saturation Data From The DST

Figure 3a shows measured temperature data in Boreholes 137–144 (see Figure 1 for borehole locations in the test block) as a function of radial distance from the borehole collar at 2 months of heating. Boreholes 137–144 lie in a vertical plane crossing the HD at about 11.9 m from the bulkhead [*CRWMS*, 1998]. The drift wall is at about 95°C after 2 months of heating. Temperatures fall rapidly with distance, except for Boreholes 139 and 143. These two boreholes are located parallel to the wing heaters (Figure 1). Since the inner wing heaters start at 1.67 m from the HD, temperatures in the first 1.67 m decline with distance in these two boreholes. Afterwards, temperatures begin to rise with distance because of the heat from the inner wing heater. At the end of the inner wing heater, temperatures drop because of the 0.66 m gap between the inner and outer wing heater. Temperatures rise again with distance along the length of the outer wing heater. Beyond the end of the outer wing heater, temperatures decline with distance, as in other boreholes.

Figure 3b shows measured temperatures in the same borehole group after 48 months of heating, i.e., toward the end of the heating phase (the total heating phase was 1503 days or approximately 49.5 months). The temperature profiles are similar in shape to those shown in Figure 3a, except that the temperatures are considerably higher because of the continued heating over four years. Additionally, three distinct zones are now evident in the temperature profile. Considering Boreholes 137–138, 140–142, and 144, there is a zone with an almost constant gradient with temperatures above 100°C. This zone extends 5–8 m from the wall of the HD. At the end of the first zone, there is a flat profile with temperatures around 96-97°C (heat pipe signatures), indicating the presence of TH coupling. At the end of the flat profile, there is a third zone with another almost constant gradient for declining temperature. The gradient of the temperature profile line in this third zone is clearly different from the one for the first zone. This change in gradient can be attributed to heat transfer through nearly dry rock in the first zone, and through wet (nearly saturated) rock in the third zone. We will shortly show that temperature data from these two zones can be used to obtain dry and wet thermal properties of the rock, respectively. Notice that there are some differences in the temperature profiles between even symmetrically located boreholes; such differences may have resulted from local heterogeneities. Temperature profile data collected from the rest of the boreholes in the other radial arrays are similar to those shown in Figures 3a and 3b, because of the symmetry of their locations, but not identical because of local heterogeneities.

To assist readers to better understand the analyses that will follow, measured temperature data in the plane of Boreholes 137-144 are shown in a different fashion in Figure 4. Instead of the line plots of Figure 3, scatter diagrams of measured temperatures in Boreholes 137-144 at 12 months (Figure 4a) and 48 months (Figure 4b) are shown in Figure 4. The width of a point in Figures 4a and 4b represents the magnitude of measured temperature at a given location, i.e., the wider a symbol in Figure 4, the larger is the temperature at the location of that symbol. For convenience, a different color has also been used to depict the magnitude of measured temperature. Note that the temperatures in the horizontal boreholes (Borehole 139 and Borehole 143) are considerably higher than those in the other boreholes because of their proximity to the wing heaters. We will use these contours of measured temperatures to locate the boiling isotherm, and subsequently, to develop an estimate of mass of water boiled, and power utilized in boiling that mass of water.

Measured temperatures at selected sensors of Boreholes 79 and 80 are shown in Figure 5. The selected sensors in Borehole 79 are 18 (~ -0.5 m from the bulkhead), 42 (23.5 m from the bulkhead or almost at the middle of the HD), and 60 (~ 41.5 m from the bulkhead), with Sensor 60 being the last RTD in Borehole 79. The selected sensors thus provide a sample of recorded temperatures at different locations along the HD. Measured temperatures at Sensors 14 (~ -0.4 m from the bulkhead), 38 (23.6 m from the bulkhead), and 60 (47.5 m from the bulkhead) of Borehole 80 are also shown in Figure 5. Sensor 60 in Borehole 80 provides measured temperatures at a location farthest from the bulkhead.

As expected, the middle of the HD (Sensor 42 of Borehole 79 and Sensor 38 of Borehole 80) records the hottest temperatures with maximum values of 160-180^{o}C. Temperature in Sensor 60 of Borehole 79, located 41.5 m from the bulkhead, also exceeds boiling temperature of water and records a maximum of ~140^{o}C. The oscillating pattern of temperature recorded at this location may have resulted from intermittent exposure to condensate flowing through an adjacent fracture. The most important feature here is the substantially lower temperature recorded by Sensor 60 of Borehole 80 (located 47.5 m from the bulkhead, at the end of the HD) compared to Sensor 60 of Borehole 79. This is because the former is located beyond the last pair of wing heaters (less heat was available at this location and hence the lower temperatures). Also, temperature at Sensor 60 of Borehole 80 remains constant at the boiling temperature of water for a long time, and exhibits a very long heat-pipe signature. It is our hypothesis that water displaced by boiling moves to the end of the HD (which is cooler) and condenses. This is also confirmed by the long heat-pipe recorded by Sensor 18 in Borehole 79 and Sensor 14 in Borehole 80, located close to the bulkhead and outside of it. This shows that most of the boiling occurs in the rockmass around the HD and the wing heaters, and not much rock is exposed to boiling conditions outside of it. Remember also that Boreholes 79 and 80, owing to their location close to the HD and wing heaters, passe through some of the hottest rock in the DST block and hence rock farther away is even less likely to encounter boiling conditions. These observations will be useful in computing the volume of water that was displaced by boiling in the DST (see below).

We next present a small subset of the DST rock saturation measurements. Figure 6 shows the volumetric water content in the rock as a function of temperature in Boreholes 79 and 80. Rock water saturation can be calculated by dividing the volumetric water content with rock porosity, which is about 11±2 percent (*BSC*, 2004). Figure 6 shows that rock water content (or saturation) remains close to ambient values until temperature reaches ~95^{o}C. Above that temperature, the rock undergoes rapid drying due to boiling till temperature reaches about 105^{o}C. Above which, the rock dries slowly until it reaches a small residual saturation. The small residual saturation may be attributed to the impact of pressure on the boiling isotherm. Ignoring that small residual water content, the observed pattern of sharp change in saturation around the boiling temperature justifies dividing the temperature data into two categories based on saturation (or water content). Temperature data from the below-boiling (< 95^{o}C) region can be used to estimate one set of thermal conductivity value, which represents the wet thermal conductivity of the rock. On the other hand, temperature data from the post-boiling period (> 100^{o}C) can be used to determine another set of thermal conductivity value, which represents the dry thermal conductivity of the rock. However, noting that drying occurs well after 100^{o}C, we will use temperature data above 110^{o}C to calculate the dry thermal conductivity of the rock. In the following, we discuss how these thermal conductivity values are estimated.

4. Analytical Solution

Figure 7 presents a schematic representation of the conceptual model developed in this section. Figure 7 also shows the coordinate system for the mathematical derivations. Assuming heat transfer by conduction only, the temperature rise ΔT (x, y, z, t) at any sensor location (x, y, z) inside the rock and at any time t can be expressed as

$$\Delta T(x, y, z, t) = \Delta T_H(x, y, z, t) + \Delta T_W(x, y, z, t), \qquad (1)$$

where ΔT_H and ΔT_W are the temperature rise due to heat emanating from the HD and the wing heaters, respectively (see Nomenclature for an explanation of the symbols). To obtain an expression for ΔT_H, we can show that the temperature rise at location (x, y, z) inside a solid, owing to an instantaneous point source of $Q\rho C$ units of heat [*Carslaw and Jaeger*, 1959, pp. 256] at location (x_o, y_o, z_o), is

$$\Delta T_H = \frac{Q}{(4\pi\alpha t)^{\frac{3}{2}}} e^{-\frac{(x-x_o)^2+(y-y_o)^2+(z-z_o)^2}{4\alpha t}}, \qquad (2)$$

where $\alpha = k/(\rho C)$. Since the HD is of length H (= 47.5 m) along the y-axis (see Figure 7), the heat source can be treated as distributed along a line of length H instead of being a point source. We can then readily write [*Carslaw and Jaeger*, 1959, pp. 258]

$$\Delta T_H = \frac{Q}{H\left(4\pi\alpha t\right)^{\frac{3}{2}}} \int_0^H e^{-\frac{(x-x_o)^2+(y-y_o)^2+(z-z_o)^2}{4\alpha t}} dy_o$$
$$= \frac{Q}{8\pi\alpha t H} e^{-\frac{(x-x_o)^2+(z-z_o)^2}{4\alpha t}} \left[erf\left(\frac{y}{2\sqrt{\alpha t}}\right) + erf\left(\frac{H-y}{2\sqrt{\alpha t}}\right) \right] . \quad (3)$$

In Equation 3, erf (η) is the error function

$$erf(\eta) = \frac{2}{\sqrt{\pi}} \int_0^{\eta} e^{-\varphi^2} d\varphi \quad (4)$$

Assuming that the polar coordinates of the points (x, z) and (x_o, z_o) are (r, θ) and (r_o, θ_o), respectively, the heat source can now be distributed over a circle with radius r_o (= 2.5 m for the HD). Equation 3 can be rewritten [*Carslaw and Jaeger*, 1959] as

$$\Delta T_H = \frac{Q}{8\pi\alpha t H} \left[erf\left(\frac{y}{2\sqrt{\alpha t}}\right) + erf\left(\frac{H-y}{2\sqrt{\alpha t}}\right) \right] \left[\frac{1}{2\pi} \int_0^{2\pi} e^{-\frac{r^2 + r_o^2 - 2rr_o \cos\theta_o}{4\alpha t}} d\theta o \right]$$
$$= \frac{Q}{8\pi\alpha t H} \left[erf\left(\frac{y}{2\sqrt{\alpha t}}\right) + erf\left(\frac{H-y}{2\sqrt{\alpha t}}\right) \right] I_0\left(\frac{rr_o}{2\alpha t}\right) e^{-\frac{r^2 + r_o^2}{4\alpha t}}, \quad (5)$$

where $r = \sqrt{(x^2 + z^2)}$ and $I_0(\eta)$ is the modified Bessel function of the first kind with order 0 and argument η. In deriving Equation 5, the following property of the modified Bessel function has been utilized [*Abramowitz and Stegun*, 1964]

$$\int_0^{2\pi} e^{\eta \cos\varphi} d\varphi = 2\pi I_0(\eta) . \quad (6)$$

Since for the DST, the source of heat is a continuous one with respect to time, we need to evaluate one more integral [*Carslaw and Jaeger*, 1959, pp. 261] to obtain the final expression

$$\Delta T_H = \frac{1}{8\pi\alpha H}\int_0^t \left[erf\left(\frac{y}{2\sqrt{\alpha(t-t_o)}}\right) + erf\left(\frac{H-y}{2\sqrt{\alpha(t-t_o)}}\right)\right] I_0\left[\frac{rr_o}{2\alpha(t-t_o)}\right] e^{-\frac{r^2+r_o^2}{4\alpha(t-to)}} \frac{\varphi(t_o)dt_o}{t-t_o}$$
$$= \frac{J_H}{4\pi kH}\int_{\frac{1}{2\sqrt{\alpha t}}}^{\infty} \left[erf(y\tau) + erf\{(H-y)\tau\}\right] I_0\left[2rr_o\tau^2\right] e^{-(r^2+r_o^2)\tau^2} \frac{d\tau}{\tau} \tag{7}$$

In Equation 7, J_H is the average of the total power up to time t provided by the canister heaters. The integral in Equation 7 obviously needs to be evaluated numerically.

Similarly, the contribution to the total temperature rise from the wing heaters *(ΔT_W)* can be obtained. It is useful to consider the wing heaters as line sources of heat. Observe that the wing heaters are located parallel to the *x*-axis at various *y* locations (see Figure 7). With Equation 2 as the starting point again, we can write the temperature rise resulting from the first pair of wing heaters as

$$\Delta T_{w1} = \frac{\mathrm{Q_W}}{(l-l_o)(4\pi\alpha t)^{\frac{3}{2}}} e^{-\frac{(y-y_o)^2+(z-z_o)^2}{4\alpha t}} \left[\int_{-l}^{-lo} e^{-\frac{(x-x_o)^2}{4\alpha t}} dx_o + \int_{lo}^{l} e^{-\frac{(x-x_o)^2}{4\alpha t}} dx_o\right]. \tag{8}$$

Since there are 25 pairs of such line sources at various *y*-locations, the total temperature rise due to these line sources is

$$\Delta T_w = \frac{\mathrm{Q_W}}{\mathrm{M}(l-l_o)(4\pi\alpha t)^{\frac{3}{2}}}\sum_{m=1}^{M} e^{-\frac{(y-y_m)^2+(z-z_o)^2}{4\alpha t}} \left[\int_{-l}^{-lo} e^{-\frac{(x-x_o)^2}{4\alpha t}} dx_o + \int_{lo}^{l} e^{-\frac{(x-x_o)^2}{4\alpha t}} dx_o\right]$$
$$= \frac{\mathrm{Q_W}}{8\pi\alpha t\mathrm{M}(l-l_o)}\sum_{m=1}^{M} e^{-\frac{(y-y_m)^2+(z-z_o)^2}{4\alpha t}} \sum_{n=1}^{4}(-1)^{n+1} erf\left(\frac{\xi_n}{2\sqrt{\alpha t}}\right) \tag{9}$$

where M is the total pairs (= 25) of wing heaters and y_m is the distance of the *m*-th wing heater from the bulkhead along the *y*-axis. In Equation 9, $\xi_1 = x + l$, $\xi_2 = x + l_0$, $\xi_3 = x - l_0$, and $\xi_4 = x - l$. Recognizing that the heat source is continuous, we need to rewrite Equation 9 as:

$$\Delta T_w = \frac{1}{8\pi\alpha\mathrm{M}(l-l_o)}\int_0^t \frac{\varphi(t_o)dt_o}{t-t_o}\sum_{m=1}^{M} e^{-\frac{(y-y_m)^2+(z-z_o)^2}{4\alpha t}} \sum_{n=1}^{4}(-1)^{n+1} erf\left(\frac{\xi_n}{2\sqrt{\alpha t}}\right) \tag{10}$$

After a change in variable, Equation 10 can also be written as:

$$\Delta T_W = \frac{J_W}{4\pi kLM} \int_{\frac{1}{2\sqrt{\alpha t}}}^{\infty} \frac{d\tau}{\tau} \sum_{m=1}^{M} e^{-\left[(y-y_m)^2+(z-z_o)^2\right]\tau^2} \sum_{n=1}^{4} (-1)^{n+1} erf(\xi_n \tau) \tag{11}$$

where J_W is the average of the total power output from the wing heaters up to time t, and L is the length of a wing heater. Similar to Equation 7, the integral in Equation 11 can be evaluated numerically. Combining Equations 1, 7, and 11, we finally obtain an expression for temperature rise at any location (x, y, z):

$$\begin{aligned}\Delta T(x,y,z,t) = {} & \frac{J_H}{4\pi kH} \int_{\frac{1}{2\sqrt{\alpha t}}}^{\infty} \left[erf(y\tau) + erf\{(H-y)\tau\} \right] I_0\left[2 r r_o \tau^2\right] e^{-(r^2+r_o^2)\tau^2} \frac{d\tau}{\tau} + \\ & \frac{J_W}{4\pi kLM} \int_{\frac{1}{2\sqrt{\alpha t}}}^{\infty} \frac{d\tau}{\tau} \sum_{m=1}^{M} e^{-\left[(y-y_m)^2+(z-z_o)^2\right]\tau^2} \sum_{n=1}^{4} (-1)^{n+1} erf(\xi_n \tau)\end{aligned} \tag{12}$$

Equation 12 is the working equation for the remainder of the analysis in this paper.

From Equation 12, it is noted that the temperature rise at any location at a specified time has a nonlinear dependency on k and α. To obtain k and α from the temperature data at the DST, we adopt the following approach. We first take the temperature data at a particular time. We then subtract the preheat temperature data from those temperature data to obtain the temperature rise during a particular interval of time. Equation 12 was then fitted to these temperature-rise data using a nonlinear fitting routine with k and α as the fitting parameters. The nonlinear fitting routine uses the Gauss-Newton algorithm with Levenberg-Marquardt [*Levenberg*, 1944; *Marquardt*, 1963] modifications for global convergence. That is, it finds the parameter values for k and α that minimize the sum of the squared differences between the observed temperature rise data at any sensor location, and those calculated using Equation 12 at the same location at any specified time. With the host rock in the DST displaying two distinct states, the wet and dry states, we will now apply our methodology to estimate k and α for both these states.

In the following, we develop the mean (or 'best fit') estimate of k and α. As a measure of the spread of the estimates around the mean, we also develop a 95% confidence interval. For calculating a 95% confidence interval (C_i), we first find the $\frac{1}{2}(1-\frac{C_i}{100}) = 0.025$ *upper critical value* (t^*) of the t-distribution for (n-1) degrees of freedom, where n is the number of temperature data points in the wet or dry zone at a given time (6 months, 12 months, etc.). For example, there are 76 temperature data points in the dry zone (temperatures larger than 110°C) at 48 months of heating in the DST. Thus, in this case, we find t^* for a t-distribution with 75 degrees of freedom, which is 1.992. The 95% confidence interval, based on a simple random sample (SRS), is then calculated as $\overline{X} \pm t^* \frac{S}{\sqrt{n}}$, where $\overline{X}$ and S are the sample mean and standard error, respectively.

5. Estimation of Uncertainties: Numerical Simulation Experiments

As stated earlier, temperature rise in the DST host rock is ultimately a function of TH coupling. Since the methodology developed in Section 4 is based on a 'conduction only' model and ignores TH coupling, it is likely to introduce some uncertainty in the thermal properties estimated from the temperature data. The issues that are of particular concern are the following. First, temperature data from the dry and wet zones are separately fitted to Equation 12 to obtain estimates of dry and wet thermal properties, respectively. It is not known how the presence of one zone (the dry or the wet) influences the estimated property of the other. Second, Equation 12 assumes a constant temperature boundary at infinity. However, the boundary of the dry zone is not at infinity and, to make the situation even more complicated, the boundary between the dry and wet zone moves dynamically (i.e., not a fixed boundary problem). Further, the boundary between the dry and wet zone is not a sharp one (water saturation changes from essentially zero at the hot end of the heat pipe to close to, or slightly higher than, ambient saturation at the cold end of the heat pipe). Third, the role of convective heat transfer is unaccounted for in Equation 12. Finally, because the DST is an open field test, a substantial amount of heat is lost (which cannot be estimated precisely), introducing more uncertainties.

To estimate the impact of these model assumptions and uncertainties on the estimated thermal properties, some numerical simulation experiments were performed. The numerical simulation experiments performed involve a simplified radial geometry (see Figure 8), rather than the complicated test geometry of the DST. However, the underlying physical problem in these numerical simulation experiments closely mimics the TH processes experienced by the unsaturated host rock of the DST. The underlying physical problem is also similar to those in Doughty and *Pruess* [1992], *Pruess et al.* [1999], and *Birkholzer* [2006a,b] in the context of investigating mass and heat flow conditions inside of and near heat pipes in geologic media.

In these numerical simulation experiments, a heat source with a constant-strength line load of 667 W/m is placed at radius r = 0 m in an infinite, homogeneous porous rock. Initially, the flow system is at steady state with no flow processes (heat, momentum, or mass) occurring; pressure, temperature, and liquid saturation have uniform values of P_i = 1 bar, T_i = 18°C, and S_{li} = 0.8. These same values are set as fixed boundary conditions at an outer boundary far enough from the heat source so as not to impact the thermal-hydrological (TH) processes near the heat source. The numerical simulator TOUGH2 [*Pruess*, 1991; *Pruess et al.*, 1999] was used to simulate the transient two-phase fluid and heat flow processes that evolve once the system starts heating up. The physical properties of the rock and the fluids involved in the numerical simulation experiments are provided in Table 2.

The plots in orange color in Figure 9a show the simulated temperature (solid line), liquid saturation (dotted line), and heat flow (dashed line) data at $t = 4$ years. Note that the heat flow data are shown as a fraction of the supplied heat. Although the selected numerical experiment is simplified, it shows all the main characteristics of coupled TH processes in unsaturated porous rock and are similar to those observed in the DST. A heat pipe, where temperature is nearly isothermal, is clearly visible between a radial distance of 2.2 m and 3.6 m. Liquid saturation is zero at the hot end (left side) of the heat pipe. At the other end of the heat pipe, liquid saturation is slightly larger than the initial saturation of 0.8. It then gradually decreases to the initial saturation as one moves farther and farther away. This indicates that water boils off at one end of the heat pipe and vapor condenses at the other end of it (condensation results in a larger-than-ambient saturation at the cold end of the heat pipe). Note that all the vapor that is generated because of boiling in this simplified problem condenses within the model. In other words, no heat loss occurs in this case.

Since the above problem involves a radial geometry and results in a substantial heat pipe signature in the temperature data (indicating TH coupling), for the sake of brevity, it will be hereafter called a radial heat pipe (RHP) scenario. In a second scenario, the RHP is slightly modified (by setting the porosity of the rock to a negligible value of 1×10^{-8} implying that no fluid phase is present in the system) to generate temperature data for a Conduction-only model. The simulated temperature (solid line) and heat flow (dashed line) data from the Conduction-only scenario are shown (in color red) in Figure 9a. Note that the grain density of the rock in this Conduction-only model is set as 2295 kg/m^3 (= 2550×0.9 kg/m^3, since porosity is 0.1 for the other scenarios) so that the mass of the rock remains the same as that in the RHP (ρ = 2550, ϕ = 0.1). Note also that, since this is a Conduction-only problem, there is no liquid saturation plot. Temperatures in the Conduction-only problem are always larger than those of the RHP. All the heat supplied in the Conduction-only problem goes into heating rock (resulting in higher temperature), whereas part of the heat in the RHP is used up in heating water (hence smaller temperature in the RHP). Note also that the temperatures in the wet zone (to the right of the heat pipe) of the RHP are only marginally different from those of the conduction-only scenario.

A source of considerable uncertainty is the amount of heat loss (and its impact on the estimated properties) from the test domain. To analyze the impact of heat loss on temperature data and estimated properties, a third scenario was simulated, which will be called the RHP-Loss scenario. This scenario is identical to the RHP, except vapor generated by boiling is allowed to leave the system. Vapor along with the latent heat of vaporization left the system, resulting in smaller temperature at any given location compared to the RHP. This is shown in Figure 9a in color blue. Observe that no heat pipe is seen in this scenario. This is because loss of vapor means that there is no condensation and refluxing of the condensate (which causes the heat pipe to exist). The rock is completely dry for r < 1.9 m and temperatures are above boiling point of water. After that, while the temperatures remain below boiling point of water, saturation gradually increases from essentially zero to ambient saturation of the rock (not seen in the plot, happens at around 30 m). This saturation pattern is different from that of the RHP. The gradual increase in saturation in the RHP-Loss case is the result of unsaturated zone flow (because of capillary suction) between rock at an ambient saturation of 0.8 and the dry rock near the heat source.

The other difference between the RHP and RHP-Loss scenarios is the pattern of heat flow. Because heat is removed at the boiling front, there is a sharp decline in the amount of heat that is carried through the boiling zone in the later scenario. For this particular problem, it has been estimated (from TOUGH2 simulations) that at $t = 4$ years about 213 W/m of heat (or approximately 31.95% of the input heat) has left the system (via vapor leaving the system). Note that this RHP-Loss scenario represents an extreme case in that vapor is allowed to leave the system completely. In the DST, however, only part of the vapor leaves the system through the open bulkhead, and thus partial condensation was still possible (evident from the existence of the heat pipes in Figure 3). This extreme scenario however will help us to illustrate the impact of TH coupling and heat loss on estimated thermal properties from temperature data.

In the above three experiments, the unsaturated rock has been assigned the same dry and wet thermal conductivity value of 2.0 W/m-K. A fourth numerical experiment was performed in which the dry rock (0% saturated) is assumed to have a thermal conductivity of 2.0 W/m-K. The wet rock (100% saturated) is assigned a thermal conductivity of 3.0 W/m-K. It is also assumed that the thermal conductivity changes linearly with saturation, i.e., $k_w = k_d + S_W\left(k_w - k_d\right)$. Since the ambient rock is assumed to be 80% saturated with water (see Table 2), the thermal conductivity of the ambient rock is thus 2.80 W/m-K. Simulated temperatures at $t = 4$ years from this fourth experiment (hereafter called RHP-Sat) are shown in Figure 9b. As a reference, simulated temperatures from the RHP are also shown in Figure 9b. At any given location, simulated temperatures in the RHP-Sat experiment are always smaller than those in the RHP experiment. This happens because of the larger wet rock thermal conductivity in the RHP-Sat experiment.

Temperature data from these four numerical simulation experiments are now fitted to a model, which is developed assuming heat transfer by conduction only. The objective of the fitting exercise is to determine the thermal properties of the rock from the simulated temperature data. If heat is introduced at a rate of q (W/m) at $r = 0$ of an infinite homogeneous solid, temperature at any location r within the solid in radial geometry after time t can be written as [*Carslaw and Jaeger*, 1959, pp. 262]

$$T = T_i - \frac{q}{4\pi k} Ei\left(-\frac{r^2}{4\alpha t}\right), \tag{13}$$

where T_i is the initial temperature and $Ei(-\zeta)$, defined as

$$-Ei(-\zeta) = \int_{\zeta}^{\infty} \frac{e^{-u}}{u} du , \tag{14}$$

is the exponential integral. Note that Equation 12 also leads to Equation 13 for $H = 0$, $r_o = 0$, and no wing heaters.

Before analyzing the estimated thermal properties from these numerical simulation experiments, let us first have a look at the input thermal diffusivity values. From Table 2, when the wet thermal conductivity is 2.0 W/m-K, the thermal diffusivity of the (thermally or hydrologically) unperturbed rock (α_{wet}), ignoring the contribution of air, is

$$\alpha_w = \frac{2}{(1-0.1)\times 2550 \times 800 + 0.1 \times 0.8 \times 998.7 \times 4187} = 9.21 \times 10^{-7} \text{ m}^2\text{/s}.$$

Similarly, when the wet thermal conductivity of the rock is 3.0 W/m-K, the thermal diffusivity of the unperturbed rock is 1.29×10^{-6} m^2/s (for a 80% saturated rock). The thermal diffusivity of the dry rock (α_{dry}), on the other hand is (again, ignoring the contribution of air)

$$\alpha_d = \frac{2}{(1-0.1)\times 2550 \times 800} = 1.09 \times 10^{-6} \text{ m}^2\text{/s}.$$

The estimated thermal properties from these numerical experiments have been summarized in Table 3. For the Conduction-only scenario, the best fit was obtained with k = 2.008 W/m-K and $\alpha = 1.089\times10^{-6}$ m^2/s. The simulated and fitted temperature rise for this problem is shown in Figure 10a (temperature rise greater than 87^{o}C, corresponding to temperatures above 105^{o}C, only are shown in this figure). The estimated thermal parameters are almost identical to the input parameters, which is expected for a conduction only scenario. For the RHP (see Figure 10a for a comparison of simulated and fitted temperature rise in the dry zone of the RHP), the estimated thermal properties are k = 2.02 W/m-K and $\alpha = 4.83\times10^{-7}$ m^2/s. While the estimated k for this zone of the RHP is within 1% of the input parameter value (= 2.0 W/m-K), the thermal diffusivity is less than half the dry rock thermal diffusivity. For the RHP-Loss scenario (see Figure 10a again for a comparison of simulated and fitted temperatures for this scenario), the estimated parameters for the dry zone is k = 2.03 W/m-K and $\alpha = 2.84\times10^{-7}$ m^2/s. While the estimated dry thermal conductivity is within 1.5% of the input value, the estimated thermal diffusivity value for the dry zone is only about 25% of the dry rock thermal diffusivity. Thus, even though the simulated temperatures include TH coupling and heat loss effects, thermal conductivity of the dry zone can be estimated within a few percentage points (most likely within 2%) of the true thermal conductivity value. The estimated thermal diffusivity value for the dry zone possibly represents an effective parameter, in which all the TH coupling effects (including moving boundaries, dynamically variable saturation effects, existence of multiple zones, etc.) are lumped together. Put in other words, the estimated thermal diffusivity value from the dry zone can be viewed as a parameter which, when used in a conduction only model such as Equations 12 or 13, will produce the same temperature data as a full TH experiment will. However, this thermal diffusivity value may not be construed as a property of the rock alone.

The simulated and fitted temperature rise in the wet zone (temperatures less than 95^{o}C or temperature rise less than 77^{o}C) for the Conduction-only, RHP, and RHP-Loss scenarios are shown in Figure 10b. For the Conduction-only scenario, of course, the estimates for the wet zone are the same as those of the dry zone. For the RHP, the estimated wet thermal conductivity (1.98 W/m-K) is about 1% smaller than the actual thermal conductivity, whereas the estimated thermal diffusivity (9.25×10^{-7} m^2/s) is virtually identical to the input parameter value. For the RHP-Loss model, the estimated thermal conductivity (1.91 W/m-K) is 4.5% smaller than the true thermal conductivity value for the wet zone and thermal diffusivity (8.96×10^{-7} m^2/s) is 2.7% smaller than the thermal diffusivity of the unperturbed rock. On the other hand, if the heat loss in this experiment was not accounted for and the entire heat load was used in Equation 13, the estimated wet thermal conductivity is 2.78 W/m-K. Thus, it appears that the uncertainty arising from our proposed approach is within acceptable limits, provided a good estimate can be obtained about the actual amount of heat carried through the test domain.

For the fourth experiment (RHP-Sat), the dry thermal conductivity is estimated as 2.03 W/m-K with a dry zone thermal diffusivity of 1.73×10^{-7} m^2/s. The estimated dry thermal conductivity is about 1.5% more than the input value, and as before, the estimated dry zone thermal diffusivity represents an effective value. The estimated wet thermal conductivity is 2.80 W/m-K, which is the thermal conductivity of an 80% saturated rock. The estimated wet zone thermal diffusivity is 1.30 W/m-K, which is similar to the input parameter of 1.29×10^{-6} m^2/s.

The observations from these numerical simulations can be summarized as follows:

(1) Dry thermal conductivity of the rock can be estimated from the temperatures in the dry zone within 1-2% of the actual value. The presence of the wet zone or the finite extent of the dry zone does not seem to impact the estimated properties in a significant way.

(2) The thermal diffusivity estimated from the dry zone temperatures represents an effective parameter, possibly combining all the effects of the TH coupling. This estimated parameter might *not* be interpreted as the thermal diffusivity of the rock.

(3) Wet thermal conductivity can be estimated from the below boiling temperatures within 1-2% uncertainty, if there is no heat loss, and within 5% uncertainty, if there is

heat loss. In other words, the uncertainty is more when there is uncertainty regarding how much heat is flowing through the rock than when TH effects are ignored.

(4) Wet thermal conductivity determined from temperatures in the below boiling zone represents the thermal conductivity of the rock at ambient saturation and *not* the thermal conductivity of the fully (100%) saturated rock.

(5) Thermal diffusivity can be estimated from the below boiling temperatures within reasonable uncertainty limits of the true value.

(6) To obtain reliable estimates of thermal properties from temperature data, reliable estimate of heat loss is needed.

The above observations will be useful in properly interpreting the estimated thermal properties from the DST temperature data. We now proceed to analyzing the temperature data from the DST with the purpose of estimating the thermal properties of the DST host rock. However, as the RHP-Loss experiment above has shown, we first need to obtain an estimate of how much heat is carried through the rock in the DST in order to obtain a reliable estimate of the thermal properties of the DST host rock. This is what is accomplished in the next section.

6. Estimation of Power Used in Heating Rock

While the total power (or energy) supplied by the heaters in the DST is known, no data are available as to what fraction of that total power is used in heating the rock. The way to resolve this is to first calculate the power that was needed to heat and boil pore water. The difference between the total supplied power and the power needed to boil water will provide a first-order estimate of the power used in heating rock. This *first-order* estimate may need further confirmation or refinement to account for uncertainties such as actual extension of the dryout zone on either side (front and back) of the HD.

The best way to calculate the volume of pore water boiled by heating is to track the boiling isotherm from measured temperature data of the DST. In Figures 4a and 4b, we have shown the contours of measured temperatures in the plane of Boreholes 137-144. In

Figure 11, we show the temperature data except that they are now divided into only two zones, one above boiling (temperature ≥ 96°C, neglecting the effect of pressure on boiling isotherm) and the other below boiling. In Figures 11a (at 12 months) and 11b (48 months), the sensors in red represent above-boiling temperatures, whereas those in blue are below boiling. The boiling isotherm (or 96°C temperature contour), which divides the temperature domain into above- and below-boiling regions, is shown in black. From Figures 11a and 11b, the volume of rock above boiling ($V_{R,AB}$) can be calculated as

$$V_{R,AB} = V_{G,AB} - V_{HD}\,, \tag{15}$$

where $V_{G,AB}$ is the geometric volume above boiling, and V_{HD} is the volume of the heated drift. The geometric area 'ABCDEFGHA' can be split into eight triangles (triangles OAB, OBC, etc., where 'O' represents the origin) as shown, and their respective areas can be calculated. When these individual triangular areas are added up, we obtain the entire geometric area. Thus, the geometric volume can be approximated as the area 'ABCDEFGHA' multiplied by the length of the HD, i.e.,

$$V_{G,AB} = \frac{H}{2}\sum_{k=1}^{8} \mathrm{mod}(z_{k+1}x_k - z_k x_{k+1})\,, \tag{16}$$

By definition, $z_9 = z_1$ and $x_9 = x_1$. The volume of the HD can be calculated as

$$V_{HD} = \pi r_o^2 H\,. \tag{17}$$

Thus, the rock volume above boiling can be obtained as

$$V_{R,AB} = \frac{H}{2}\sum_{k=1}^{8} \mathrm{mod}(z_{k+1}x_k - z_k x_{k+1}) - \pi r_o^2 H \tag{18}$$

In evaluating Equation 18, remember that (x_k, z_k) and (x_{k+1}, z_{k+1}) are functions of the time of observation (as illustrated in Figures 11a and 11b). The power in kW (P_{HBW}) required for heating the water to boiling temperature (T_b) from its ambient temperature (T_a) and providing the latent heat of vaporization (λ) is then calculated as

$$P_{HBW} = \phi V_{R,AB} S_W \rho_W \left[\frac{C_{pW}(T_b - T_a) + \lambda}{1000 t_{obs}} \right] \tag{19}$$

where the symbols have their usual meaning and t_{obs} is the time of observation in seconds (from the start of heating at the DST). The power in kW (P_{HR}) used to heat rock till $t = t_{obs}$ is then

$$P_{HR} = P_T - P_{HBW} \tag{20}$$

Using the measured boiling point isotherm from the DST (similar to the ones shown in Figures 11a and 11b) we calculated the power utilized in heating rock in steps of six months. The results, along with the actual total heating power from the heaters (P_T), are shown in Table 4. Apart from the small uncertainty associated with estimating the above-boiling rock volume from the estimated areas in Equation 16, some uncertainty remains regarding the length of the dryout zone along the drift axis (we have used *H*, the length of the HD, in Equation 18 as a first estimate). Since there are no measured temperature data beyond the end of the HD (Sensor 60 of Borehole 80 is at the end of the HD), the extent of the dryout zone on either side (front or back) of the HD is not known precisely. However, temperature data shown in Figure 5 indicate that the two ends of the HD are substantially cooler than the middle of the HD, and that mostly condensation of the boiled water (displaced from the dryout zone) occurs at those locations. Thus, it can be inferred that the dryout zone may not extend much beyond the HD (on either side). Still, it is possible that some boiling (and hence drying) occurs beyond the end of the HD.

Since no direct data are available, we turn to modeling studies of the DST in order to resolve the above uncertainty. Elaborate three-dimensional (3-D) TH models have been previously developed to analyze the thermal and hydrological data from the DST [*Birkholzer and Tsang*, 2000; *Mukhopadhyay and Tsang*, 2003; *Birkholzer et al.*, 2005]. These 3-D DST TH models are based on the TOUGH2 finite-integral numerical simulator [*Pruess*, 1991; *Pruess et al.*, 1999], and use the dual-permeability approach [*Pruess*, 1991] to model the flow and transport of water, vapor, air, and heat in unsaturated fractured rock. Based on these 3-D TH models, and using the average of the actual heating power at the DST as input to the 3-D TH model (see Table 1), we developed contours of temperature in different vertical planes around the HD at different times. Figure 12 shows the contours of temperatures at 48 months (when the dryout zones are supposedly near the maximum) in three vertical planes: 2.7 m before (Figure 12a), 0.25 m after (Figure 12b), and 4.5 m after (Figure 12c) the end of the HD. Notice the large difference in the extent of the dryout zone between Figures 12a and 12b. This difference is, as explained earlier, because of the absence of any heat source beyond the end of the HD. Figure 12c confirms that drying virtually does not occur beyond a few meters from the end of the HD. Thus, using the length of the HD as the extent of the dryout zone in Equation 18 may not have introduced a large uncertainty (say, not more than a few %).

As further confirmation, we calculated the power used in heating rock in the DST model domain using the simulated temperature data from the 3-D TH model. The approach for accomplishing this and partial results (up to 27 months of heating at the DST) have been previously published [*Mukhopadhyay and Tsang*, 2003]. Here, we present the same results through 48 months of heating (in steps of six months) in Table 4, which also shows the power used in heating rock as obtained from the observed boiling isotherms (Equation 20). Note that the difference between them is never more than 4.2 kW (i.e. < 2% of the maximum total power). This last observation leads us to conclude that either estimate can be used as input for Equation 12 with an understanding that an error of 5% or less may be introduced in doing so. We thus estimate thermal conductivity of the DST rock using the rock heating power obtained from the DST TH model (since this accounts for boiling beyond the HD), and carry out sensitivity analyses by varying the input heating power in Equation 12 by ±5%.

7. Results

For the purposes of our analysis, we will assume that the rock at any location is dry if the temperature is equal to or more than 110^{o}C. In other words, it is assumed that all the water from the pore spaces has been boiled away by the time the temperature exceeds 110^{o}C, which is supported by Figure 6 (neglecting the small residual saturation above

110^{o}C). On the other hand, we will assume a rock to be in wet condition if the temperature is equal to or below 95^{o}C, which is again supported by the measured saturation versus temperature data in Figure 6. This last assumption implies that large-scale boiling at the DST begins only above that temperature, and the water content of the rock is ambient before boiling begins.

7.1 Dry Thermal Properties

The boundaries of the dry and wet zones in the DST change dynamically with the progress of heating. At initial phases of heating, there is no dry zone. As heating continues, a small dry zone is formed near the HD and along the wing heaters. With further heating, the dry zone continues to expand, pushing the wet zone farther and farther away from the heat source. As an example, see the radial location of the boundary of the dry zone as recorded by the sensors in Boreholes 137, 138, and 139 at various times (Table 5). These three boreholes are representative samples of the data in the DST host rock, with Borehole 137 oriented vertically upwards, Borehole 138 oriented upwards at an angle of 45^o with the HD, and Borehole 139 oriented horizontally. In Table 5, the distances are listed as those from the center of the HD along the orientation of the borehole under consideration. For example, at 12 months of heating, the boundary of the dry zone is located at 3.51 m in Borehole 137, 3.92 m in Borehole 138, and 13.1 m in Borehole 139 as measured from the center of the HD. This implies that, at 12 months of heating, any location closer than 3.51 m along Borehole 137 is recording a temperature of more than 110^{o}C. By 24 months of heating, the dryout zone has expanded to 5.0 m in Borehole 137, 6.02 m in Borehole 138, and 14.0 m in Borehole 139. Towards the end of the heating phase at the DST (i.e., at 48 months), the dryout zone is located at 6.8 m, 8.12 m, and 14.9 m in Boreholes 137, 138, 139, respectively.

Because of this dynamically changing location of the dryout zone boundary, the analytical solution in Equation 12 has to be applied over different spatial extents at different times in order to obtain estimates of the dry thermal conductivities. For example, at 24 months of heating, we need to consider temperature data from sensors located at 5.0 m or closer from the HD in Borehole 137. For estimating the thermal properties of the dry state, we consider temperature data from the DST at 30, 36, 42 and 48 months of heating. The extent of the dryout zone was somewhat limited earlier than 30 months. Temperature data earlier than 30 months were thus not considered for the estimation of dry thermal properties. In Figures 13a and 13b, we show the measured temperatures in Boreholes 137, 138, and 139, along with the 'best fit' estimates of the calculated temperatures, at 36 and 48 months of heating.

In Table 6, the parameter values for k and α in the dry rock that produce the best fit with measured temperatures at various times are provided. As a measure of goodness of fit, the 95% confidence interval for both those parameters are also given in Table64. The best-fit thermal conductivity values fall in the range 1.31–1.50 W/m-K. This estimate of the dry thermal conductivity value is 10-21% lower than that of 1.67 W/m-K, which has been used in earlier TH modeling of the DST [*Birkholzer and Tsang*, 2000; *Mukhopadhyay and Tsang*, 2003]. The value of 1.67 W/m-K was obtained from laboratory-scale core measurements [*Brodsky et al*., 1997]. This possibly indicates the difference between a point estimate (based on a core sample) from a certain location and a mean for the entire location.

In order to obtain a spatial distribution of the thermal conductivities of the repository horizon at Yucca Mountain, *Ramsey et al*. (2004) performed extensive geostatistical simulations. They selected a three-dimensional cubic model [*Hsu et al*., 1995] for thermal conductivity of a porous medium. In this model, thermal conductivity is a function of porosity, thermal conductivity of the fluid in the pore space, thermal conductivity of the solid matirx, and the geometry and connectivity of the solid. *Ramsey et al*. [2004] treated the thermal conductivity of the fluid as constant but the remaining model parameters were treated as spatially uncertain random functions. They then employed sequential Gaussian simulation to develop 50 equally likely realizations of those uncertain parameters. Thermal conductivity measurements of *Brodsky et al*. [1997] and petrophysical measurements (for porosity) were used to condition these uncertain properties. Through these elaborate geostatistical simulations, they generated spatial distribution of thermal conductivity values for various stratigraphic layers and computed the mean thermal conductivity (both wet and dry) for each of those layers. Our estimate of (1.31-1.50 W/m-K) the dry thermal conductivity is similar to the mean dry thermal conductivity value of 1.42 W/m-K (with a standard deviation of 0.265 W/m-K) estimated by *Ramsey et al*. [2004] through those geostatistical simulations

7.2 Wet Thermal Properties

Before start of heating, the entire DST host rock can be considered as wet rock. With constant heating, as the dryout zone expands outwards with continuous boiling of pore water, the wet zone is pushed away from the heat source. The inner boundary of the wet zone, located at the HD at the beginning of heating, moves away from the HD (the outer boundary of the wet zone remains at infinity, or at the end of the instrumentation boreholes for our purposes). In Table 7, we show the location of the inner boundary of the wet zone at various times. Recollect that we have defined the wet zone as any sensor location recording 95^{o}C or lower. The inner boundary of the wet zone is thus the contour of 95^{o}C temperatures. For example, in Borehole 137, the inner boundary of the wet zone can be found at a radial location of 7.4 m and 10.39 m at 24 months and 48 months of heating, respectively. At those same times, the 95^{o}C contours were located at 15.79 m and 17.59 m, respectively, in Borehole 139. In other words, the extent of the wet zone is different in different boreholes at different times.

In Figure 14a, we show measured temperature increases in Boreholes 137–139 within the wet zone, i.e., wherever temperature was below 95^{o}C at 12 months of heating. In the same figure, we also show the computed temperature increases in those boreholes using the best-fit parameters for the wet zone. Figure 14b is similar to Figure 14a, except that the results are shown at 24 months of heating. In Table 8, the estimated parameter values are tabulated along with 95% confidence intervals for those parameters at various times. Observe that the estimated wet thermal conductivity is mostly in the range 2.02–2.18 (W/m-K), except at six months when the estimated wet thermal conductivity is 1.92 (W/m-K). This estimate is again different (by about 1-9%) from the wet thermal conductivity of 2.0 W/m-K used in earlier TH analyses [*Birkholzer and Tsang*, 2000; *Mukhopadhyay and Tsang*, 2003], as obtained from *Brodsky et al*. [1997]. The geostatistical simulations of *Ramsey et al*. [2004], on the other hand, yielded a mean wet thermal conductivity of 2.07 W/m-K (with a standard deviation of 0.252 W/m-K).

7.3 Sensitivity Analyses

Temperature rise in the host rock of the DST is dependent upon the total heat utilized for heating the rock. Since some uncertainty exists in determining what fraction of the input heat is actually used for heating the rock, uncertainties exist in the estimated (dry and wet) thermal conductivity values. In this section, we present results to demonstrate the sensitivity of the estimated thermal conductivity values to uncertainty in the heat used for heating the rock. As indicated earlier, sensitivity analyses are carried out by varying the heat used for raising rock temperature by ±5%.

Table 9 shows estimated best-fit dry thermal conductivity values at various times with different heat inputs. The second column in Table 9 shows the best-fit dry thermal conductivity with 95% of the heat shown in Table 4, whereas the fourth column shows the same with 105% of the heat shown in Table 4. The third column is reproduced from Table 6 for easy comparison. Similarly, Table 10 shows the best-fit wet thermal conductivities at various times. From Tables 9 and 10, it is evident that reducing the heat input by 5% results in almost a 5% reduction in the estimated thermal conductivity values. Similarly, increasing the heat input by 5% results in a similar increase in the estimated thermal conductivity values. This almost linear dependency is expected (see Equation 12). The estimated dry and wet thermal conductivity values (after varying the heat input) are not dissimilar to the 95% confidence interval around the best-fit obtained using the heat listed in Table 2 as input to our model. It thus can be concluded that, even after assuming a ±5% uncertainty (which is more than that indicated by measured data) in estimating the heat used for raising the temperature in the DST host rock, the temperature data produce a consistent estimate of thermal conductivity. Since these estimates have been obtained using actual temperature data from the DST over a wide spatial and temporal range, they possibly represent 'upscaled' thermal conductivities of the host rock (as opposed to point observation through core measurements). The validity of our estimates is further confirmed by the observation of *Ramsey et al*. [2004] through geostatistical simulations. Moreover, the results, based on physical processes alone, presented in this paper possibly provide the first independent verification of upscaled thermal conductivities of the repository host rock at Yucca Mountain.

8. Summary

The large volume of temperature data collected from the DST provides an opportunity to estimate the field-scale thermal conductivity of the host rock. In this paper, we provide an efficient methodology for estimating the field-scale thermal conductivities of the host rock from temperature data. This method derives the thermal conductivities from actual temperature data collected over large spatial and temporal scale and does not use the core measurements as input.

The thermal regime in the DST host rock can be described in terms of "wet" and "dry" zones. At the beginning of heating, the entire host rock was about 85-90% saturated with water and could be called "wet". With progress of heating, as water started boiling, a dryout zone appeared, and expanded with further heating. At the end of heating, although the wet zone was still present, there was a considerable dryout zone near the HD. Temperature data from the DST clearly established these wet and dry zones (including a two-phase zone as well). Temperature data also established the fact that thermal conductivities were different in the dry and wet zones.

We have developed an analytical solution for transient temperature rise in the DST host rock. This analytical solution has two components: rise in temperature caused by heat emanating from the canister heaters and that caused by heat coming from the wing heaters. This analytical solution was then separately fitted to measured temperatures in the dry and wet zones at various times of data collection. We report the best-fit estimates from the exercise as the field-scale thermal conductivity for the dry and wet rock. We also provide the 95% confidence level for our estimates. As expected, our field-scale estimates are somewhat different from small-scale core measurement values [*Brodsky et al*., 1997], and are more consistent with the findings of *Ramsey et al*. [2004].

It is possible that, since the analytical solution developed in this paper is based on an assumption of heat transfer by conduction only, the estimated thermal properties may have uncertainties because they are derived from temperature data, which contain coupled TH effects. We performed four numerical simulation experiments with simplified radial geometry; however, the underlying physical processes in these experiments were similar to those experienced by the host rock of the DST. From these controlled experiments, we could conclude that the estimated thermal properties were within reasonable limits of uncertainty. The impact of ignoring the presence of convective heat transfer or the two-phase did not appear to have a significant impact on the estimated thermal conductivities. The same was true for the thermal diffusivity estimated from the temperatures in the wet zone. On the other hand, it turned out the thermal diffusivity estimated from the temperatures in the dry zone could not be construed as a property of the rock, but might be interpreted as an effective parameter representing the lumping of all the TH effects into one parameter. These numerical simulation experiments thus provided a useful set of guidelines while interpreting the estimated thermal properties from the DST temperature data. The numerical simulation experiments also illustrated the impact of uncertainty in estimating the heat loss from the test domain on the estimated thermal properties.

As illustrated by the numerical simulation experiments, a likely source of uncertainty in our estimates of the DST thermal properties is the amount of energy actually used in heating the rock. By tracking the boiling isotherm in the DST temperature data, we showed that no more than a 5% uncertainty exists in this regard. Thus, as a sensitivity analysis, we obtained the range of thermal conductivity (both dry and wet) that would result from a ±5% uncertainty in input heat. The range is mostly within the 95% confidence limit of the best-fit estimates.

Nomenclature

C Specific heat capacity of the rock, J/kg-K.

C_i Confidence interval.

C_{pW} Specific heat capacity of water, J/kg-K.

H Length of the HD, m.

J_H Average of total power from the HD, W.

J_W Average of total power from the wing heaters, W.

k Thermal conductivity, W/m-K.

k_d Dry thermal conductivity, W/m-K.

k_w Wet thermal conductivity, W/m-K.

l x-coordinate of the end of the wing heater, m.

l_o x-coordinate of the start of the wing heater, m.

L Length of a wing heater, m.

M Pairs of wing heaters.

n Number of measurements.

P_{HBW} Power required for heating and boiling of water, kW.

P_{HR} Power required for heating rock, kW.

P_T Total power, kW.

q Linear heat load in Equation 13, W/m.

Q Strength of point source of heat, m^3-K.

r Radial location, m.

r_o Radius of the HD, m.

S Sample standard error, W/m-K for thermal conductivity or m^2/s for thermal diffusivity.

S_W Water saturation.

T Temperature, ^oC.

T_a Ambient temperature, ^oC.

T_b Boiling temperature, ^oC.

ΔT Total temperature rise, ^oC.

ΔT_H Temperature rise due to heat coming from the HD, ^oC.

ΔT_W Temperature rise due to heat coming from the wing heaters, ^oC.

t Time, s.

t^* Upper critical value of a t-distribution with (n-1) degrees of freedom.

t_{obs} Observation time, s.

u Dummy variable in Equation 14.

V_{HD} Volume of the HD, m^3.

$V_{G,AB}$ Geometric volume of the rock above boiling, m^3.

$V_{R,AB}$ Volume of the rock above boiling, m^3.

$\overline{X}$ Sample mean, W/m-K or m^2/s.

x x-coordinate, m.

x_k x-coordinate of point 'k', m.

x_{k+1} x-coordinate of point '$k+1$', m.

x_o x-coordinate of point source of heat, m.

y y-coordinate, m.

y_m y-coordinate of the m-th wing heater, m.

y_o y-coordinate of point source of heat, m.

z z-coordinate, m.

z_k z-coordinate of point 'k', m.

z_{k+1} z-coordinate of point '$k+1$', m.

z_o z-coordinate of point source of heat, m.

α Thermal diffusivity of the rock, m^2/s.

α_d Thermal diffusivity of dry rock, m^2/s.

α_w Thermal diffusivity of wet rock, m^2/s.

ϕ Porosity.

λ Latent heat of vaporization for water, J/kg.

ρ Density of the rock, kg/m^3.

ρ_W Density of water, kg/m^3.

τ Dimensionless time.

ζ Dummy variable in Equation 13.

Acknowledgments

We thank the anonymous reviewers of the Water Resources Research for their careful and critical review of the manuscript. We thank Yu-Shu Wu, Keni Zhang, and Dan Hawkes of the Ernest Orlando Lawrence Berkeley National Laboratory (Berkeley Lab) for their constructive review of the draft manuscript. Permission provided by Richard Carlson of Lawrence Livermore National Laboratory in using Figure 6 is duly acknowledged. This work was supported by the Director, Office of Civilian Radioactive Waste Management, U.S. Department of Energy, through Memorandum Purchase Order EA9013MC5X between Bechtel SAIC Company, LLC, and Berkeley Lab. The support is provided to Berkeley Lab through the U.S. Department of Energy Contract No. DE-AC03-76SF00098.

References

Abramowitz, M. and Stegun, I. A. (eds.) (1964), *Handbook of Mathematical Functions*, National Bureau of Standards, Washington, District of Columbia.

BSC (2004), Thermal Testing Measurements Report, TDR-MGR-HS-000002 REV 00, Bechtel SAIC Company, Las Vegas, Nevada.

Birkholzer, J.T. (2006a), Estimating liquid fluxes in thermally perturbed fractured rock using measured temperature profiles, *Journal of Hydrology*, 327, 496-515.

Birkholzer, J.T. (2006b), A temperature-profile method for estimating flow in geologic heat pipes, Journal of Contaminant Hydrology, 85, 89-117.

Birkholzer, J.T. and Y.W. Tsang, (2000), Modeling the thermal-hydrologic processes in a large-scale underground heater test in partially saturated fractured tuff, *Water Resources Research*, 36 (*6*), 1431-1447.

Birkholzer, J.T., S. Mukhopadhyay, and Y.W. Tsang (2005), Drift-Scale Coupled Processes (DST and TH Seepage) Models, MDL-NBS-HS-000015 REV02, Bechtel SAIC Company, Las Vegas, Nevada.

Brodsky, N. S., M. Riggins, J. Connolly, J., and P. Ricci (1997), Thermal expansion, thermal conductivity, and heat capacity measurements for boreholes UE25 NRG-4, UE25 NRG-5, USW NRG-6, and USW NRG-7/7,. SAND95-1955 UC-814, Sandia National Laboratory, Albuquerque, New Mexico.

Carslaw, H. S. and J.C. Jaeger (1959), *Conduction of Heat in Solids*, Oxford University Press, New York, New York.

CRWMS (1998), Drift Scale Test As-Built Report, BAB000000-01717-5700-00003 REV 01, CRWMS M&O, Las Vegas, Nevada.

CRWMS (2000), Thermal Tests Thermal-Hydrological Analyses/Model Report, ANL-NBS-TH-000001 REV 00, CRWMS M&O, Las Vegas, Nevada.

Doughty, C. and K. Pruess (1992), A similarity solution for two-phase water, air, and heat flow near a linear heat source in a porous medium, *J. Geophys. Res*., 97 (B2), 1821-1838.

Engelhardt, I., S. Finsterle, and C. Hofstee (2003), Experimental and numerical investigation of flow phenomena in nonisothermal, variably saturated bentonite-crushed rock mixtures, *Vadose Zone Journal*, 2, 239-246.

Finsterle, S (1999), ITOUGH2 User's Guide, LBNL-40040 UC 400, Lawrence Berkeley National Laboratory, Berkeley, California.

Gehlin, S. (1998), Thermal Response Test – In-Situ Measurements of Thermal Properties in Hard Rock, Ph.D. Thesis, Lulea University of Technology, Lulea, Sweden.

Kolditz, O. and C. Clauser, (1998), Numerical simulation of flow and heat transfer in fractured crystalline rocks: application to the hot dry rock site in Rosemanowes, Geothermics, 27, 1-23.

Lehmann, H., K. Wang, and C. Clauser, (1998), Parameter identification and uncertainty analysis for heat transfer at the KTB drill site using a 2-D inverse method, Tectonophysics, 291, 179-194.

Levenberg, K (1944), A method for the solution of certain nonlinear problem in least squares, Quart. Appl. Math., 2, 164-168.

Marquardt, D. W. (1963), An algorithm for least squares estimation of nonlinear parameters, SIAM J. Appl. Math., 11, 431-441.

Mukhopadhyay, S. and Y.W. Tsang (2003), Uncertainties in coupled thermal-hydrological processes associated with the Drift Scale Test at Yucca Mountain, Nevada, Journal of Contaminant Hydrology, 62-63, 595-612.

Pruess, K. (1991), TOUGH2—A General-Purpose Numerical Simulator for Multiphase Fluid and Heat Flow, LBNL-29400, Lawrence Berkeley National Laboratory, Berkeley, California.

Pruess, K., C.M. Oldenburg, and G.J. Moridis (1999), TOUGH2 User's Guide, Version 2.0, LBNL-43134, Lawrence Berkeley National Laboratory, Berkeley, California.

Ramsey, J., J. Bean, C. Lum, and E. Hardin (2004), Thermal Conductivity of the Potential Repository Horizon, MDL-NBS-GS-000005 REV01, Bechtel SAIC Company, Las Vegas, Nevada.

Tsang, Y. W., J.T. Birkholzer, B. Freifeld, J. Peterson, M.Q. Hu, E.L. Sonnenthal, and N. Spycher (1999), Yucca Mountain Single Heater Test Final Report, LBNL-42537, Lawrence Berkeley National Laboratory, Berkeley, California.

Vosteen, H-D, V. Rath, C. Clauser, and B. Lammerer (2003), The thermal regime of the eastern Alps from inversion analyses along the TRANSALP profile, Physics and Chemistry of the Earth, 28, 393-405.

Figure Captions

Figure 1. Schematic diagram of the HD, the wing heaters, and the RTD temperature holes in the DST

Figure 2. History of total input power in the DST

Figure 3a. Measured temperatures in Boreholes 137-144 at two months of heating

Figure 3b. Measured temperatures in Boreholes 137-144 at 48 months of heating. The spike in temperature in Borehole 144 at ~10 m is because of a malfunctioning RTD

Figure 4a. Scatter and contour diagram of measured temperatures in Boreholes 137-144 at 12 months of heating

Figure 4b. Scatter and contour diagram of measured temperatures in Boreholes 137-144 at 48 months of heating

Figure 5. Measured temperatures as a function of time in selected sensors of Boreholes 79 and 80

Figure 6. Rock moisture content versus temperature as measured from neutron logging of Boreholes 79 and 80 (with permission from Richard Carlson, Lawrence Livermore National Laboratory)

Figure 7. Schematic diagram of the coordinate system used in developing conceptual model of conductive heat transfer at the DST

Figure 8. Schematic diagram of the one-dimensional radial geometry employed in the numerical experiments of Section 5. This figure shows the TH conditions in the unsaturated porous rock at some unspecified time after the start of heating

Figure 9a. TOUGH2-simulated temperatures, liquid saturation, and heat flow rate from the numerical experiments in Section 5 as a function of radial distance from the heat source. The red lines correspond to the Conduction-only experiment, the orange lines correspond to the RHP model, and the blue lines correspond to the RHP-Loss model. In each of these plots, temperatures are represented by solid lines, liquid saturation by dash-dotted lines, and heat flow by dashed lines

Figure 9b. TOUGH2-simulated temperatures for the RHP and RHP-Sat numerical experiments

Figure 10a. Simulated and fitted temperatures in the dry zone of the Conduction-only, RHP, and RHP-Loss numerical experiments in Section 5

Figure 10b. Simulated and fitted temperatures in the wet zone of the Conduction-only, RHP, and RHP-Loss numerical experiments in Section 5

Figure 11a. Construction of the boiling isotherm from measured temperatures at 12 months in the plane of Boreholes 137-144

Figure 11b. Construction of the boiling isotherm from measured temperatures at 48 months in the plane of Boreholes 137-144

Figure 12a. Contours of simulated temperatures at 48 months in a vertical plane 0.5 m before the end of the HD (47 m from the bulkhead)

Figure 12b. Contours of simulated temperatures at 48 months in a vertical plane 0.5 m after the end of the HD (48 m from the bulkhead)

Figure 12c. Contours of simulated temperatures at 48 months in a vertical plane 1.5 m after the end of the HD (49 m from the bulkhead)

Figure 13a. Measured and estimated temperature rise in the dry zone in Boreholes 137-139 at 36 months of heating

Figure 13b. Same as Figure 13a but at 48 months of heating

Figure 14a. Measured and estimated temperature rise in the wet zone in Boreholes 137-139 at 12 months of heating

Figure 14b. Same as Figure 14a but at 24 months of heating

Table Captions

Table 1. Average input power at the DST at various times

Table 2. Parameters and properties used in the numerical experiments in Section 4.

Table 3. Summary of estimated thermal parameters from the numerical simulation experiments in Section 4. Note that the input wet thermal conductivity for

the unperturbed rock (80% saturated) in the RHP-Sat experiment is 2.80 W/m-K. The wet thermal conductivity of 3.0 W/m-K is for a 100% saturated rock.

Table 4. Total power, and comparison of power used for heating rock as obtained from Equation 20 and *Mukhopadhyay and Tsang* [2003] at various times

Table 5. Radial location of measured 100^{o}C temperature contours in Boreholes 137, 138, and 139

Table 6. Estimated dry thermal properties of the fractured welded tuff of Tptpmn at Yucca Mountain, Nevada

Table 7. Radial location of measured 95^{o}C temperature contours in Boreholes 137, 138, and 139

Table 8. Estimated wet thermal properties of the fractured welded tuff of Tptpmn at Yucca Mountain

Table 9. Estimated dry thermal properties with 95%, 100%, and 105% of the input heat shown in Table 4

Table 10. Estimated wet thermal properties with 95%, 100%, and 105% of the input heat shown in Table 4

Table 1

Time (months)	Average of Total Canister Heater Power (kW)	Average of Total Wing Heater Power (kW)	Average of Total Heating Power (kW)
0–6	51.67	134.70	186.37
0–12	52.09	133.26	185.35

0–18	52.07	132.15	184.22
0–24	51.43	129.86	181.29
0–30	50.96	128.65	179.61
0–36	49.86	125.62	175.48
0–42	48.76	122.36	171.12
0–48	47.70	119.43	167.13

Table 2.

Parameter	Value
Applied Heat load	
$q\left(r \to 0\right)$	667 W/m
Initial Conditions and Boundary Conditions ($r \to \infty$)	
Pressure P_i	1 bar
Temperature T_i	18°C
Saturation S_{li}	0.8
Properties of the Porous Medium	
Permeability K	2×10^{-14} m^2
Porosity ϕ	0.1
Grain density ρ	2550 kg/m^3
Grain heat capacity C	800 J/kg-K
Wet thermal conductivity k_w	2.0 W/m-K
Wet thermal conductivity k_w for RHP-Sat (100% saturated)	3.0 W/m-K
Dry thermal conductivity k_d	2.0 W/m-K
Characteristic curves of the porous medium	
Capillary pressure P_C	$-\frac{1}{\theta}\left[\left(S^*\right)^{-1/\nu}-1\right]^{1-\nu}$
Relative permeability of liquid K_{rl}	$\sqrt{S^*}\left[1-\left(1-(S^*)^{1/\nu}\right)^{\nu}\right]^2$
Realtive permeability of gas, K_{rg}	1-K_{rl}

van Genuchten parameter S^*	$\frac{S_l - S_{lr}}{1 - S_{lr}}$
Residual liquid saturation S_{lr}	9.6×10^{-4}
van Genuchten parameter $(1/\theta)$	0.125 bar
van Genuchten parameter ν	0.45
Maximum capillary pressure $P_{C,\,max}$	5000 bars
Thermodynamic properties of water and vapor	
Density of water ρ_W (at 1 bar and 18^{o}C)	998.7 kg/m^3
Specific heat capacity of water C_{pW}	4187 J/kg-K
Specific latent heat of vaporization λ	2.268×10^3 J/kg

Table 3

Numerical Experiment	Actual k (W/m-K)		Estimated k (W/m-K)		Actual α ($\times10^7$) (m^2/s)		Estimated α ($\times10^7$) (m^2/s)	
	Dry	Wet	Dry	Wet	Dry	Wet	Dry	Wet
Conduction-only	2.0	2.0	2.008	2.008	10.9	10.9	10.89	10.89
RHP	2.0	2.0	2.02	1.98	10.9	9.21	4.83	9.25
RHP-Loss	2.0	2.0	2.03	1.91	10.9	9.21	2.84	8.96
RHP-Sat	2.0	3.0	2.03	2.80*	10.9	12.9	1.73	13.0

Table 4

Time (months)	Average of Total Heating Power (kW)	Estimated Power for Heating Rock (from Equation 18) (a) (kW)	Estimated Power for Heating Rock[1] (b) (kW)	Difference (b-a) (kW)
0 – 6	186.37	143.2	144.7	1.5
0 – 12	185.35	138.1	139.0	0.9
0 – 18	184.22	133.6	137.8	4.2
0 – 24	181.29	132.3	135.4	3.1
0 – 30	179.61	130.1	133.3	3.2
0 – 36	175.48	129.3	129.6	0.3
0 – 42	171.12	128.0	126.5	1.5
0 – 48	167.13	122.3	123.1	0.8

Table 5

Time (months)	Distance of 110^{o}C Contours from the Center of the HD (m) Along		
	Borehole 137	Borehole 138	Borehole 139
6	2.61	2.72	8.6
12	3.51	3.92	13.1
18	4.11	5.12	13.7
24	5.00	6.02	14.0
30	5.60	6.92	14.6
36	5.90	7.52	14.9
42	6.20	7.82	14.9
48	6.80	8.12	14.9

[1] From TOUGH2 simulations of the DST [*Mukhopadhyay and Tsang*, 2003]

Table 6

Time (months)	Estimated Parameter Values for dry conditions			
	Dry Thermal Conductivity, k_d (W/m-K)		Thermal Diffusivity, α (m^2/s)	
	Best Fit	95% Confidence Interval	Best Fit	95% Confidence Interval
30	1.31	1.26-1.36	$0.36x10^{-6}$	$0.33x10^{-6}$—$0.39x10^{-6}$
36	1.41	1.37-1.48	$0.38x10^{-6}$	$0.35x10^{-6}$—$0.42x10^{-6}$
42	1.44	1.38-1.51	$0.37x10^{-6}$	$0.33x10^{-6}$—$0.41x10^{-6}$
48	1.50	1.43-1.56	$0.39x10^{-6}$	$0.35x10^{-6}$—$0.434x10^{-6}$

Table 7

Time (months)	Radial Distance of 95^{o}C Contours from the Center of the HD (m)		
	Borehole 137	Borehole 138	Borehole 139
6	3.51	3.92	13.40
12	4.71	5.41	14.60
18	5.60	7.22	15.20
24	7.40	9.01	15.79
30	8.30	9.62	16.39
36	8.90	10.83	16.99
42	9.79	12.03	16.99
48	10.39	12.34	17.59

Table 8

	Estimated Parameter Values for wet conditions

Time (months)	Estimated Parameter Values for wet conditions			
	Best Fit	95% Confidence Interval	Best Fit	95% Confidence Interval
6	1.92	1.85-1.99	1.055×10^{-6}	1.017×10^{-6}—1.094×10^{-6}
12	2.18	1.99-2.38	1.073×10^{-6}	0.979×10^{-6}—1.169×10^{-6}
18	2.15	2.00-2.31	1.099×10^{-6}	1.007×10^{-6}—1.191×10^{-6}
24	2.02	1.88-2.16	0.969×10^{-6}	0.902×10^{-6}—1.036×10^{-6}
30	2.16	1.99-2.33	1.039×10^{-6}	0.951×10^{-6}—1.127×10^{-6}
36	2.13	1.98-2.29	1.050×10^{-6}	0.967×10^{-6}—1.132×10^{-6}
42	2.03	1.91-2.15	1.007×10^{-6}	0.941×10^{-6}—1.073×10^{-6}
48	2.09	1.93-2.24	1.049×10^{-6}	0.958×10^{-6}—1.141×10^{-6}

Table 9

Time (months)	Best-fit Dry Thermal Conductivity (W/m-K)		
	0.95*Heat in Table 2	Heat in Table 2	1.05*Heat in Table 2
30	1.26	1.31	1.36
36	1.35	1.41	1.48
42	1.36	1.44	1.51
48	1.42	1.49	1.57

Table 10

Time (months)	Best-fit Wet Thermal Conductivity (W/m-K)		
	0.95*Heat in Table 2	Heat in Table 2	1.05*Heat in Table 2
6	1.82	1.92	2.02
12	2.07	2.18	2.29
18	2.04	2.15	2.25
24	1.92	2.02	2.12
30	2.05	2.16	2.27
36	2.02	2.13	2.24
42	1.93	2.03	2.12
48	1.99	2.09	2.19

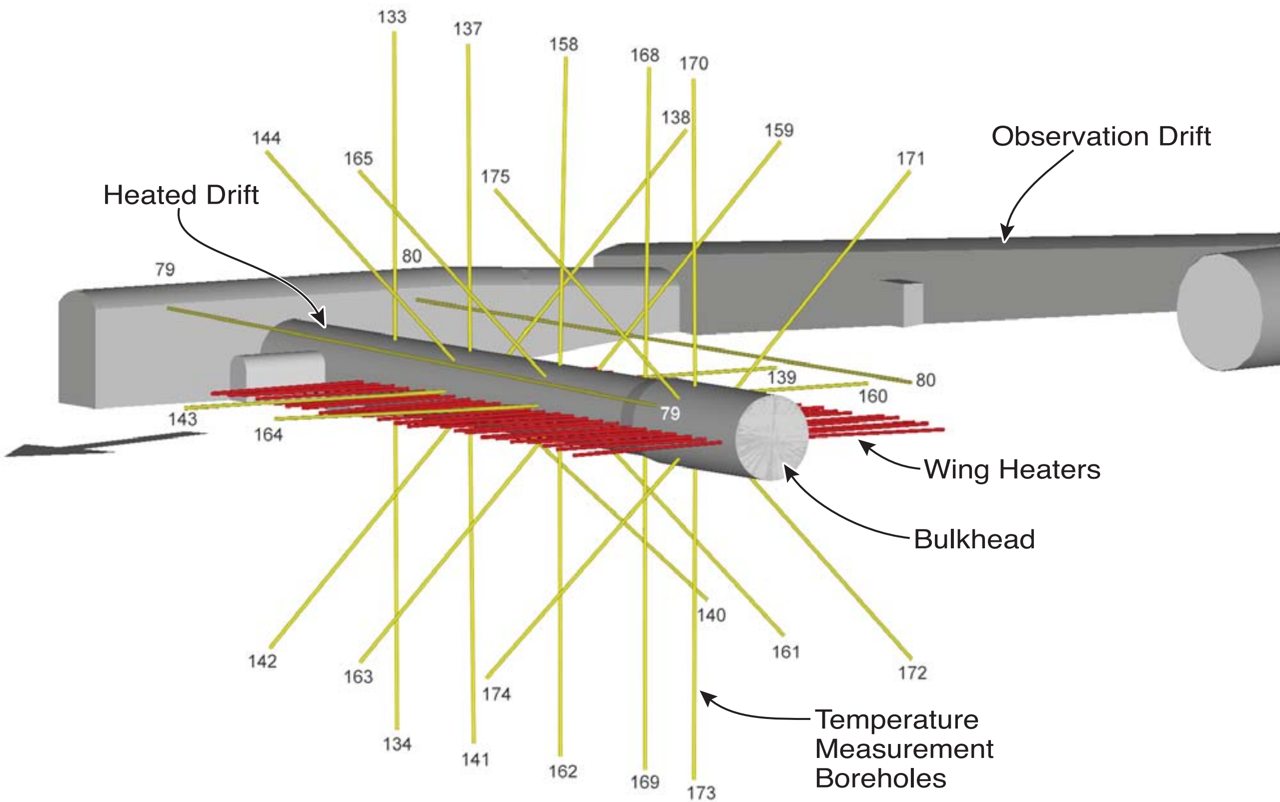

133
137
158
168
170
138
159
144
165
175
171
Observation Drift
Heated Drift
79
80
139
80
160
79
143
164
Wing Heaters
Bulkhead
140
161
172
142
163
174
134
141
162
169
173
Temperature
Measurement
Boreholes

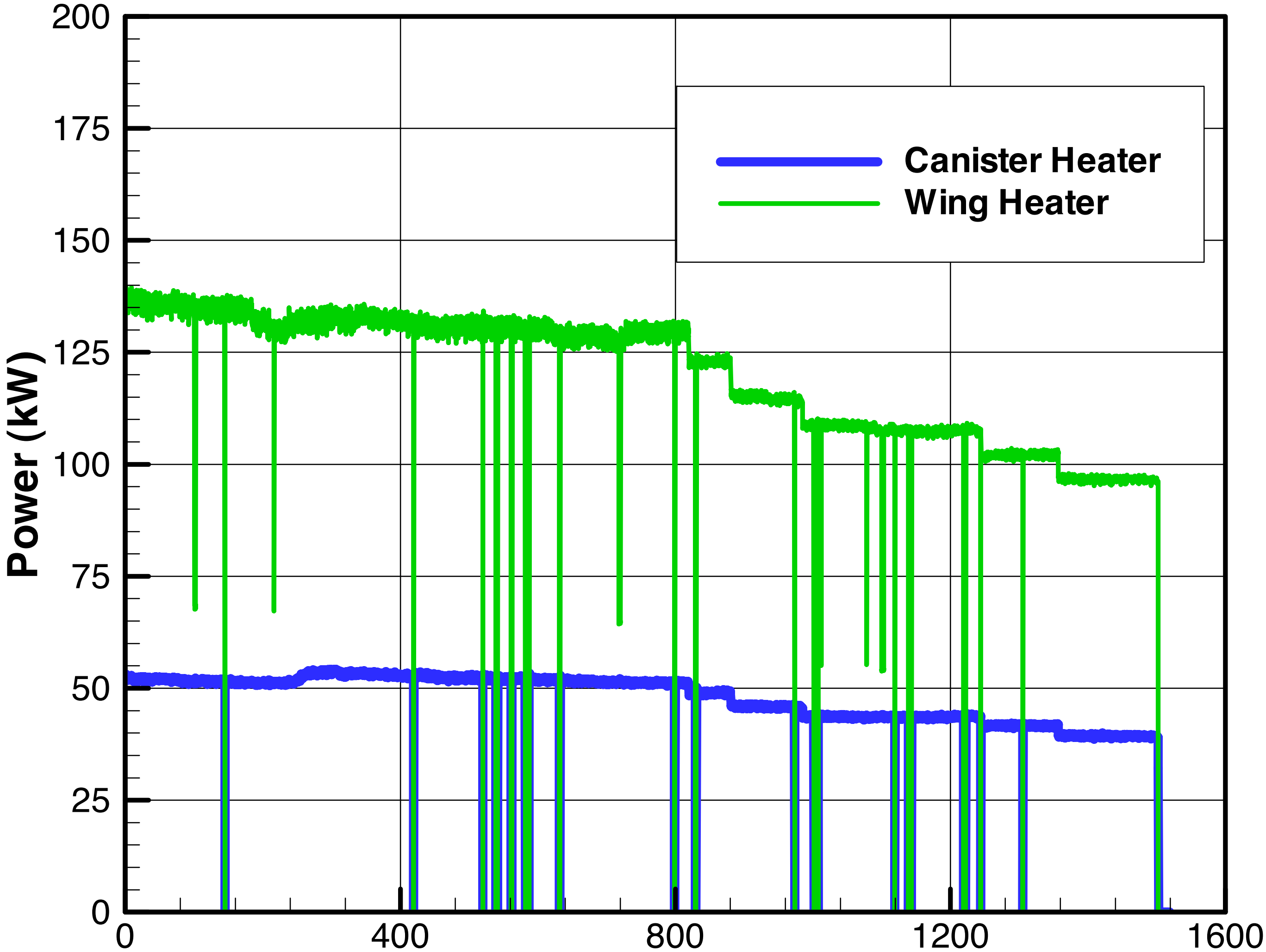
Canister Heater
Wing Heater
Power (kW)
Time (days)
0
25
50
75
100
125
150
175
200
0
400
800
1200
1600

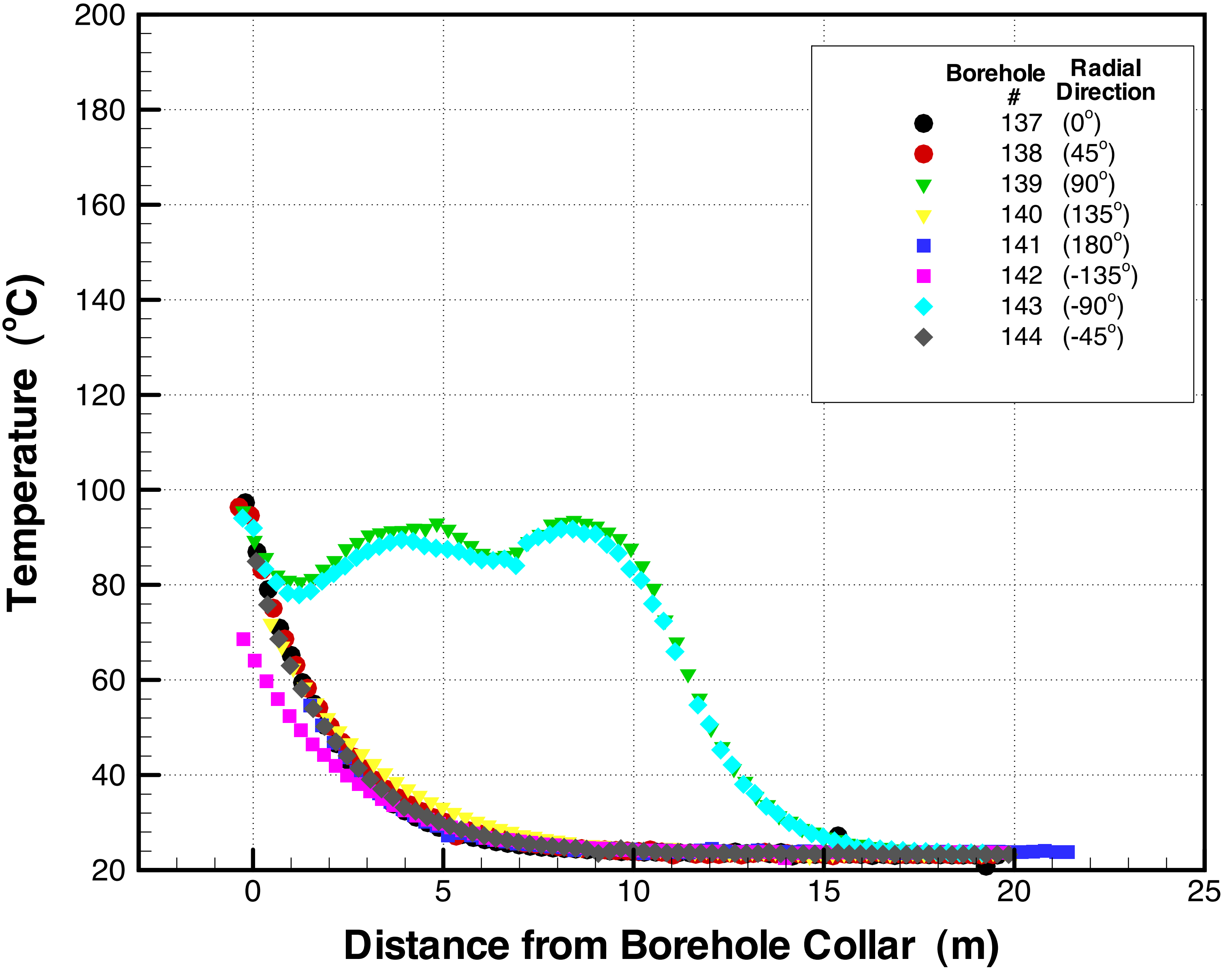

Borehole #
Radial Direction
137 (0°)
138 (45°)
139 (90°)
140 (135°)
141 (180°)
142 (-135°)
143 (-90°)
144 (-45°)
Temperature (°C)
Distance from Borehole Collar (m)
200
180
160
140
120
100
80
60
40
20
0
5
10
15
20
25

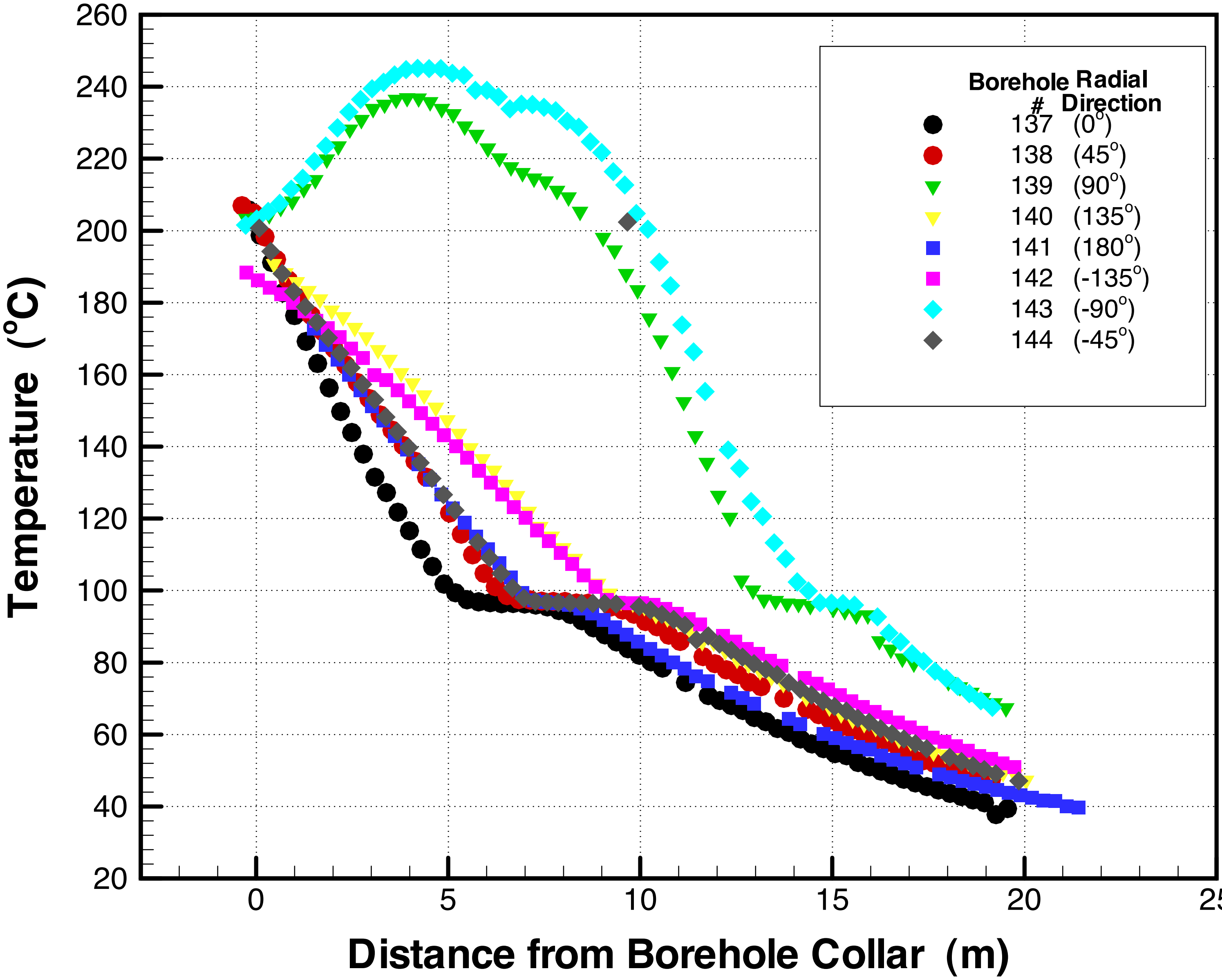

Borehole #
Radial Direction
137 (0°)
138 (45°)
139 (90°)
140 (135°)
141 (180°)
142 (-135°)
143 (-90°)
144 (-45°)
Temperature (°C)
260
240
220
200
180
160
140
120
100
80
60
40
20
0
5
10
15
20
25
Distance from Borehole Collar (m)

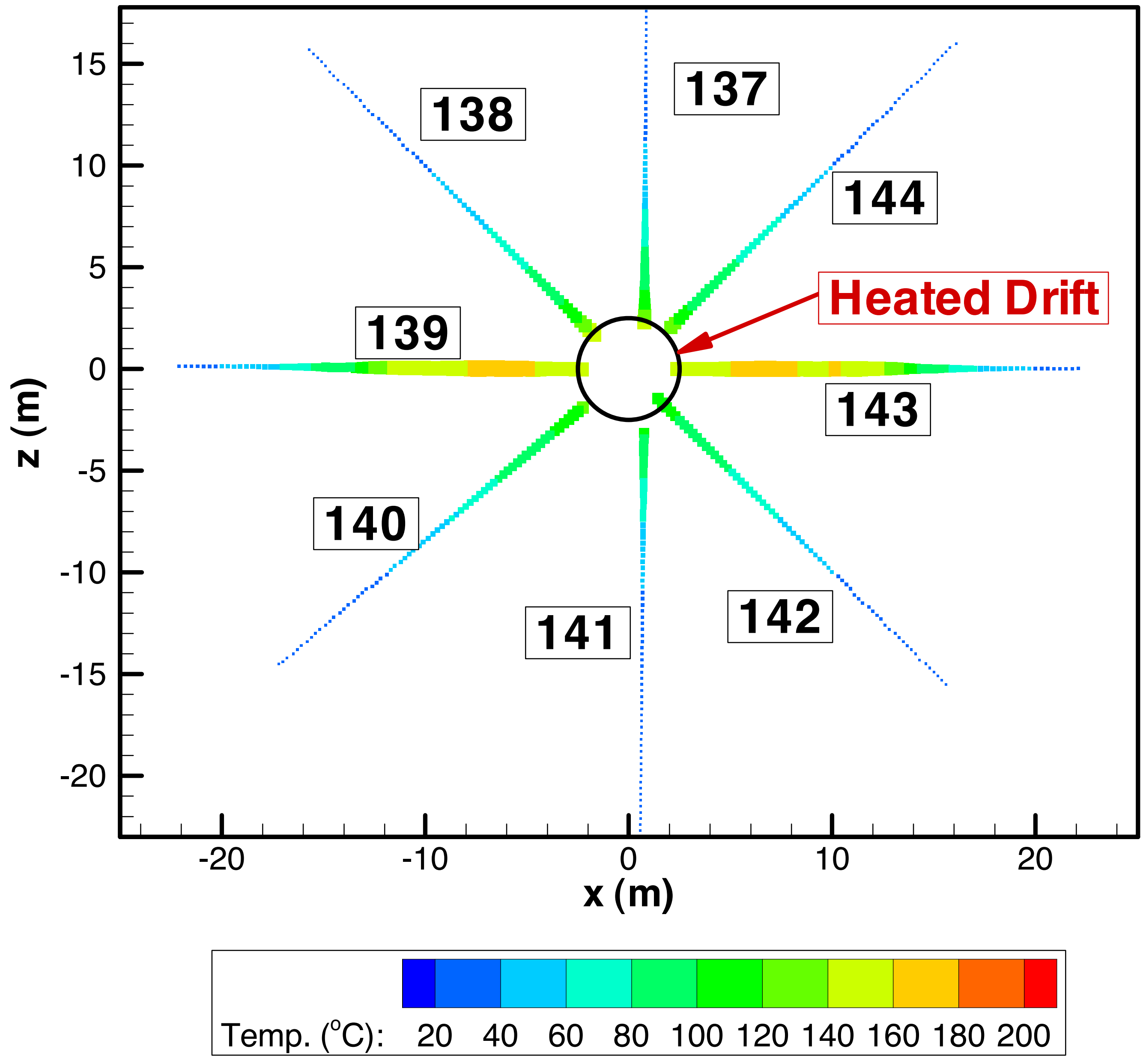

138
137
144
Heated Drift
139
143
140
141
142
z (m)
x (m)
15
10
5
0
-5
-10
-15
-20
-20
-10
0
10
20
Temp. (°C): 20 40 60 80 100 120 140 160 180 200

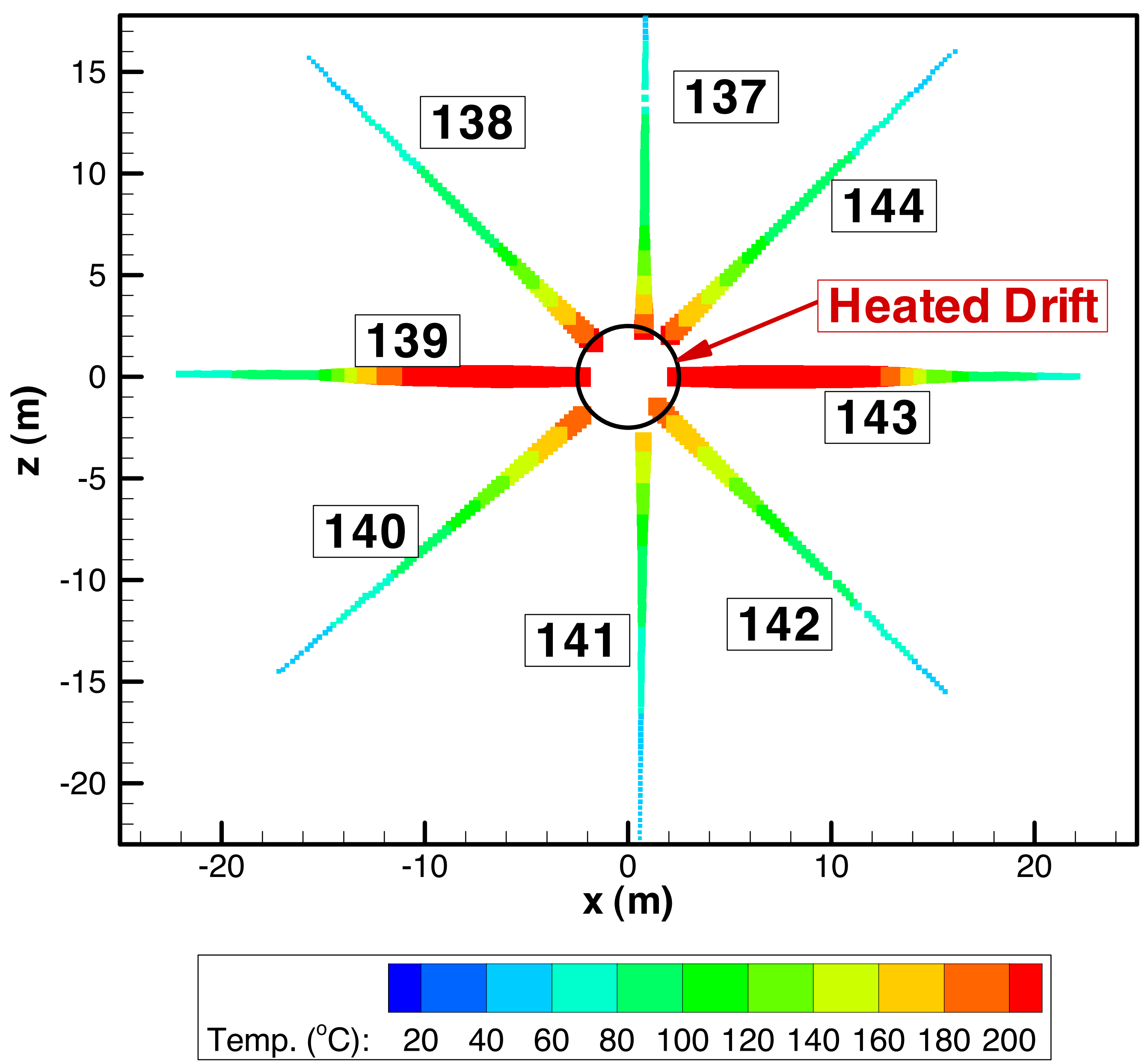
137
138
144
Heated Drift
139
143
140
141
142
15
10
5
0
-5
-10
-15
-20
z (m)
-20
-10
0
10
20
x (m)
Temp. (°C): 20 40 60 80 100 120 140 160 180 200

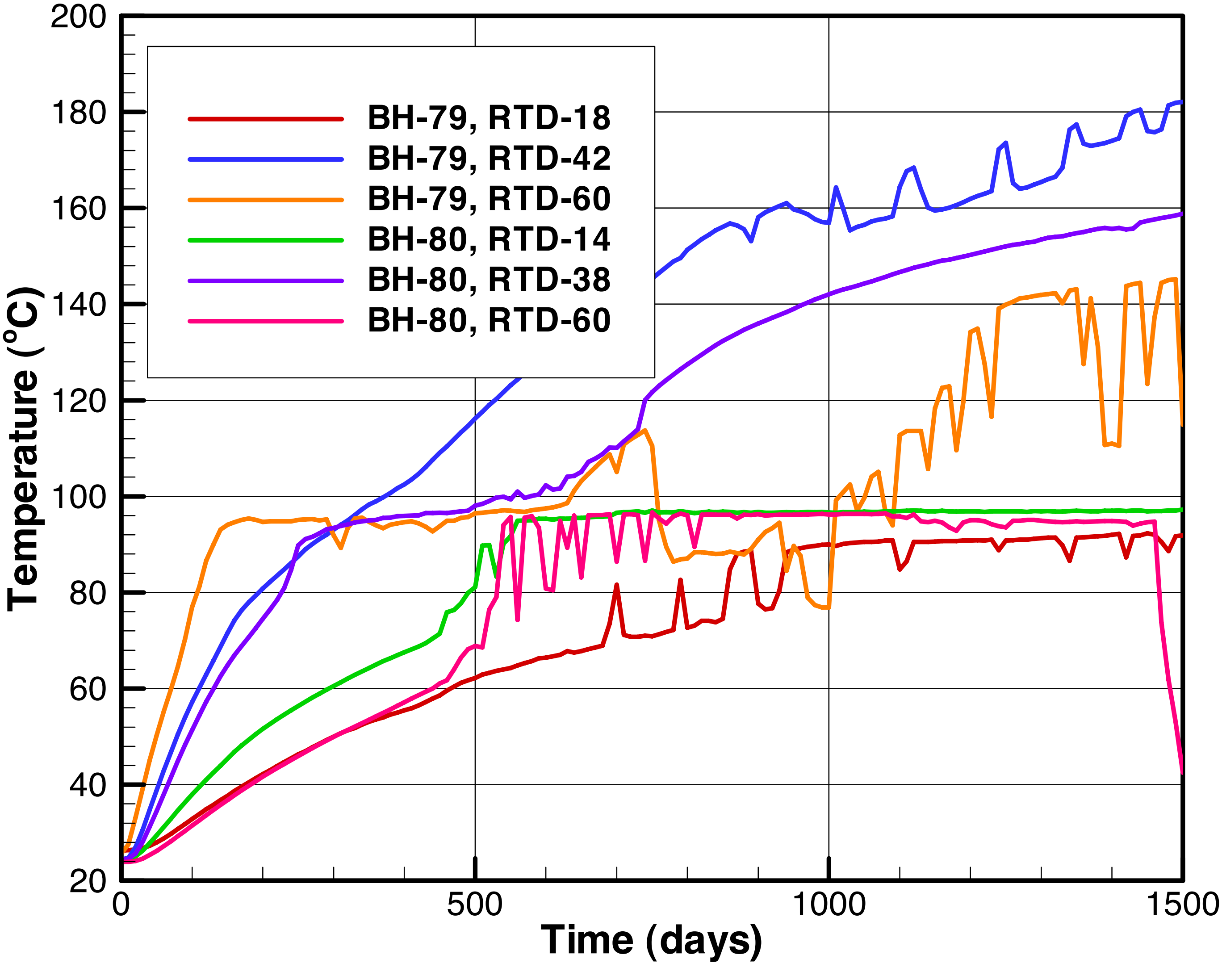

BH-79, RTD-18
BH-79, RTD-42
BH-79, RTD-60
BH-80, RTD-14
BH-80, RTD-38
BH-80, RTD-60
Temperature (°C)
Time (days)
200
180
160
140
120
100
80
60
40
20
0
500
1000
1500

DST Neutron Logging and Temperature Measurements From Boreholes 79 and 80

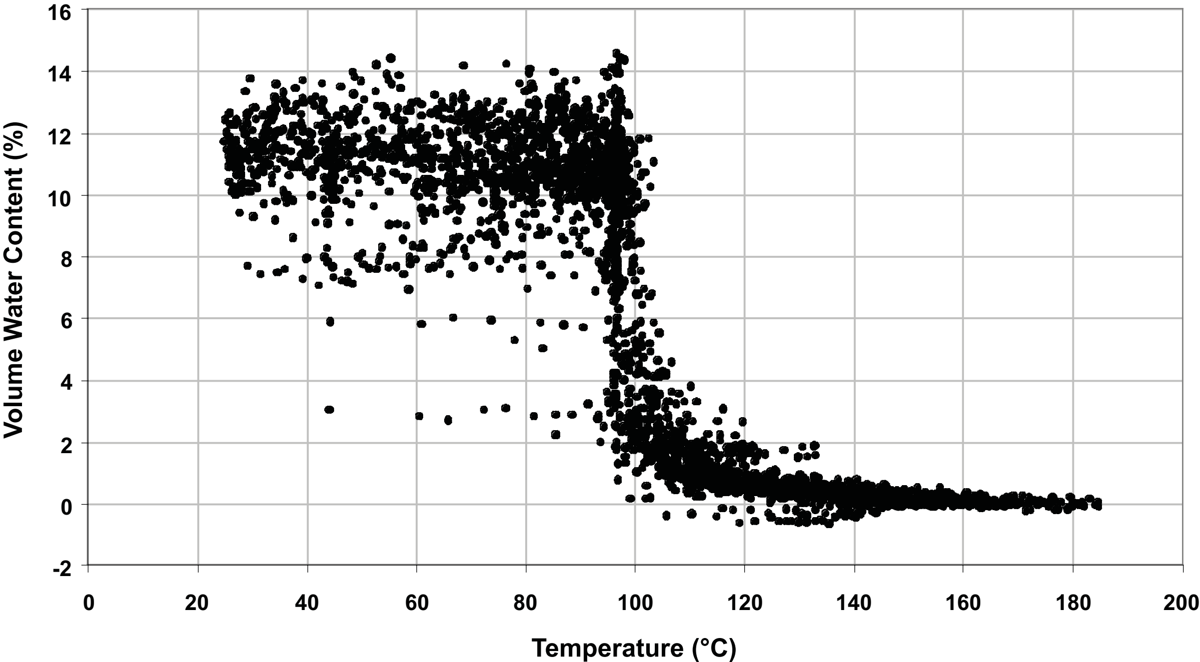

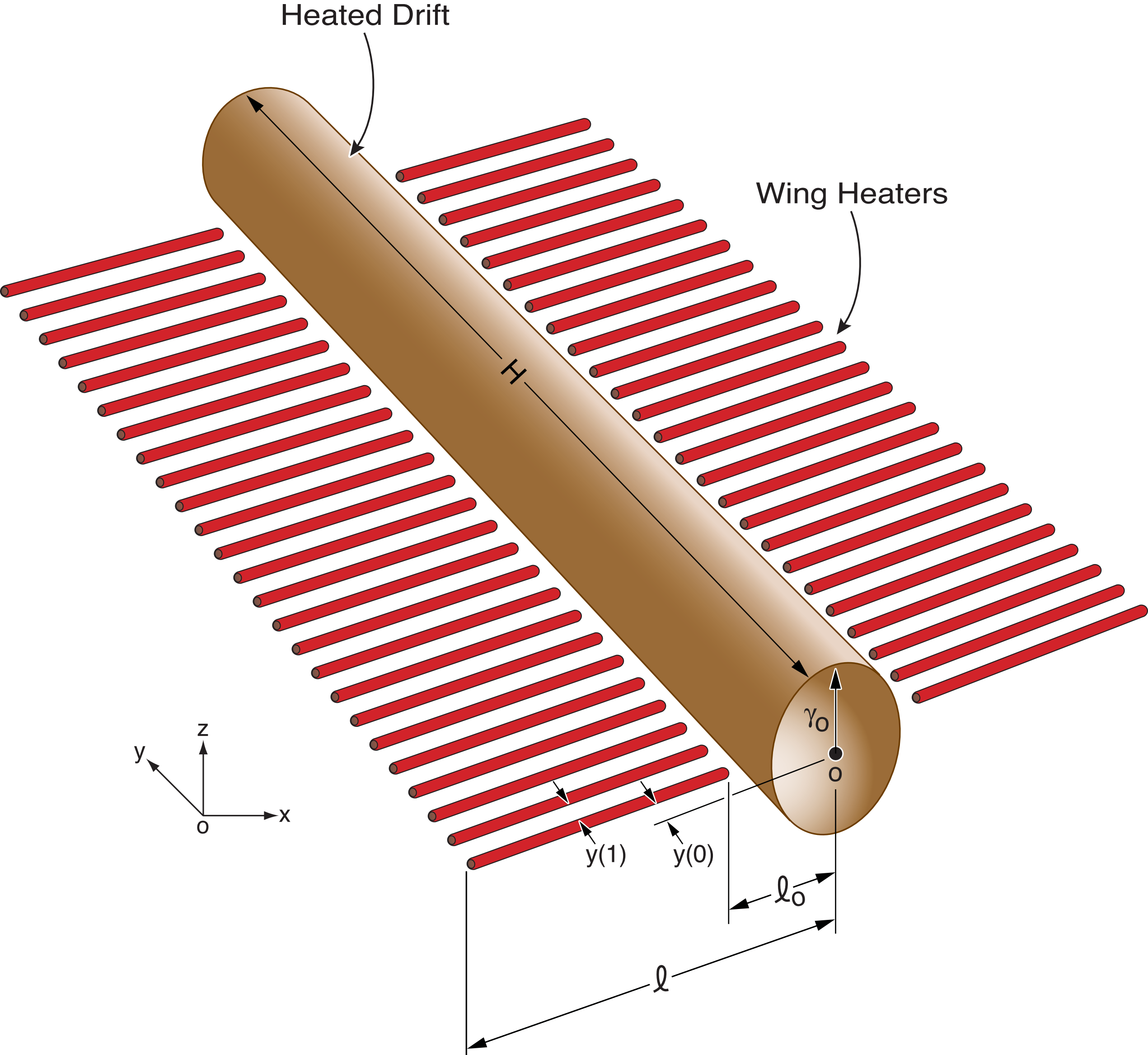
Heated Drift
Wing Heaters
H
γ_o
o
y(1)
y(0)
ℓ_o
ℓ
z
y
x
o

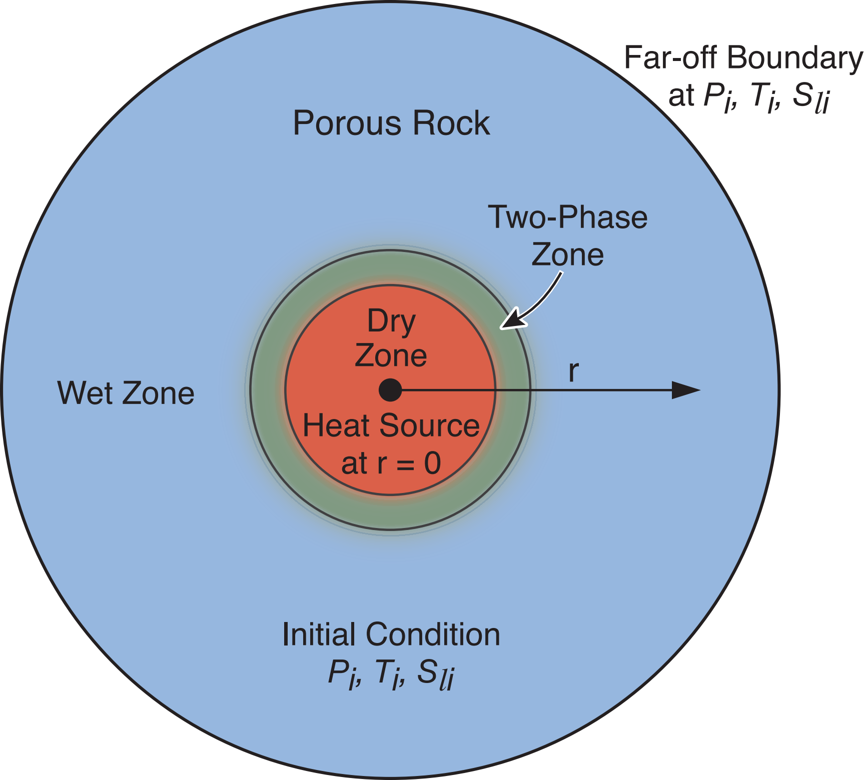

Far-off Boundary
at P_i, T_i, S_{li}
Porous Rock
Two-Phase
Zone
Dry
Zone
r
Wet Zone
Heat Source
at r = 0
Initial Condition
P_i, T_i, S_{li}

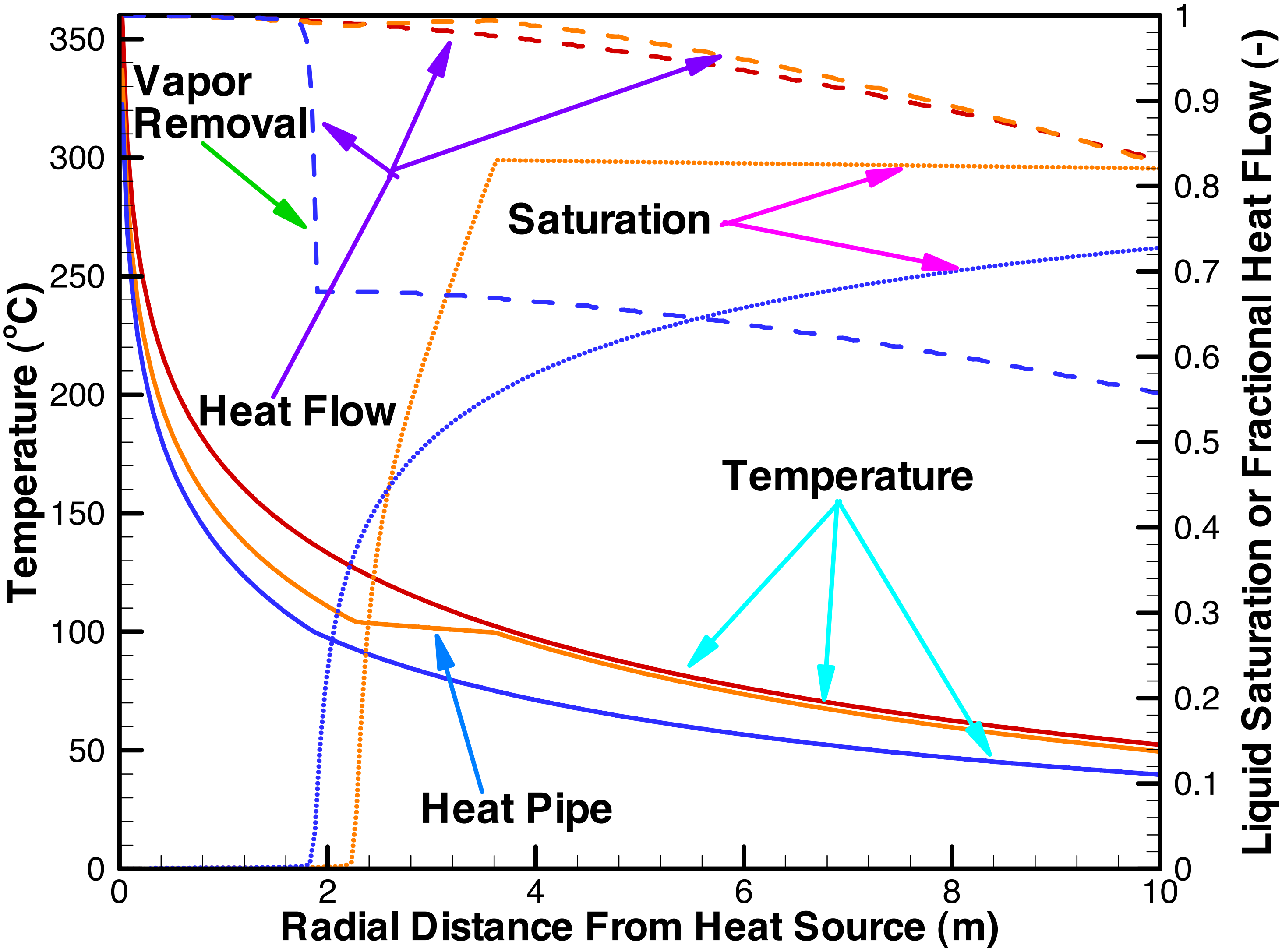

Vapor
Removal
Heat Flow
Saturation
Temperature
Heat Pipe
Temperature (°C)
Radial Distance From Heat Source (m)
Liquid Saturation or Fractional Heat FLow (-)
0
50
100
150
200
250
300
350
0
2
4
6
8
10
0.1
0.2
0.3
0.4
0.5
0.6
0.7
0.8
0.9
1

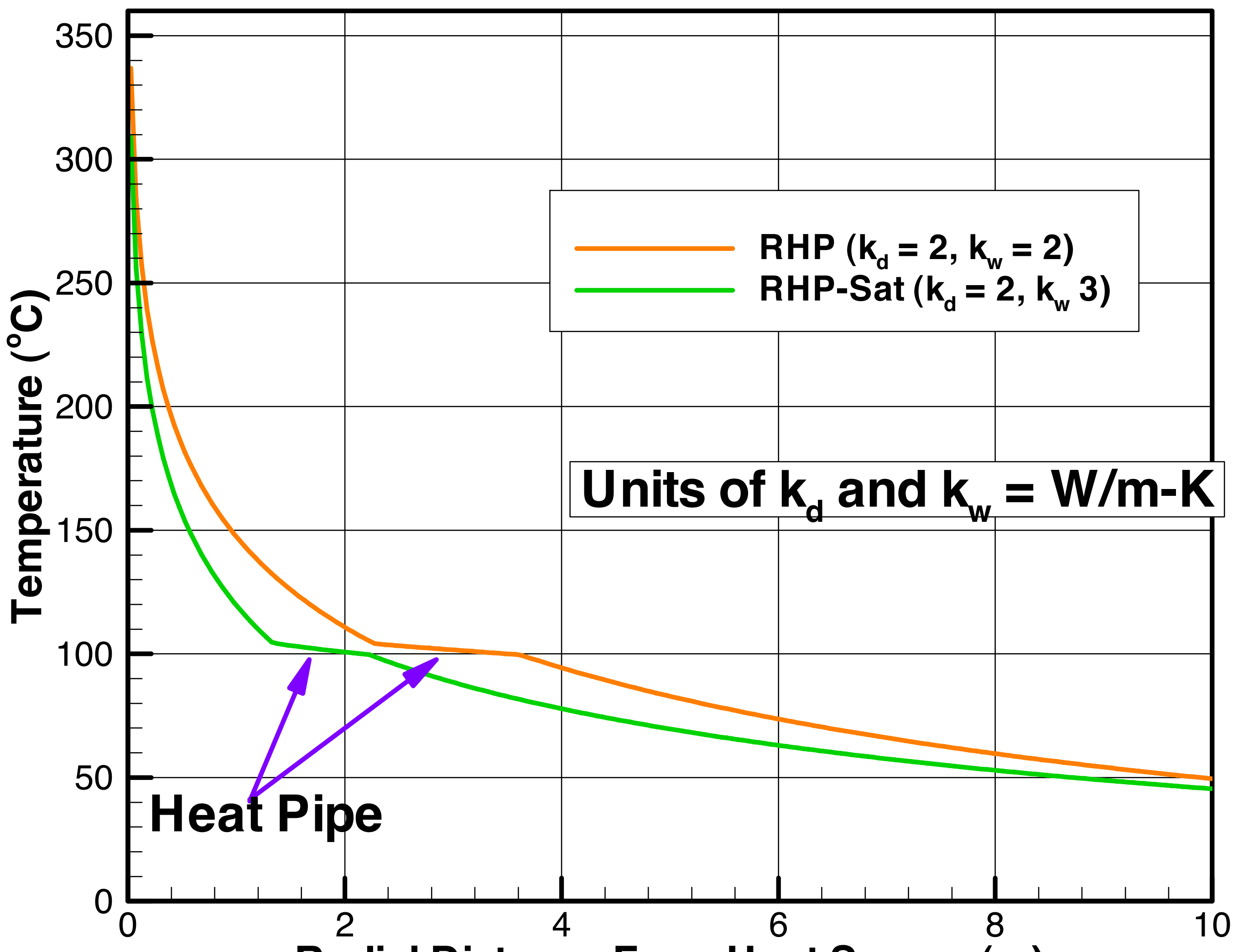

350
300
250
200
150
100
50
0
Temperature (°C)
0
2
4
6
8
10
Radial Distance From Heat Source (m)
RHP (k_d = 2, k_w = 2)
RHP-Sat (k_d = 2, k_w 3)
Units of k_d and k_w = W/m-K
Heat Pipe

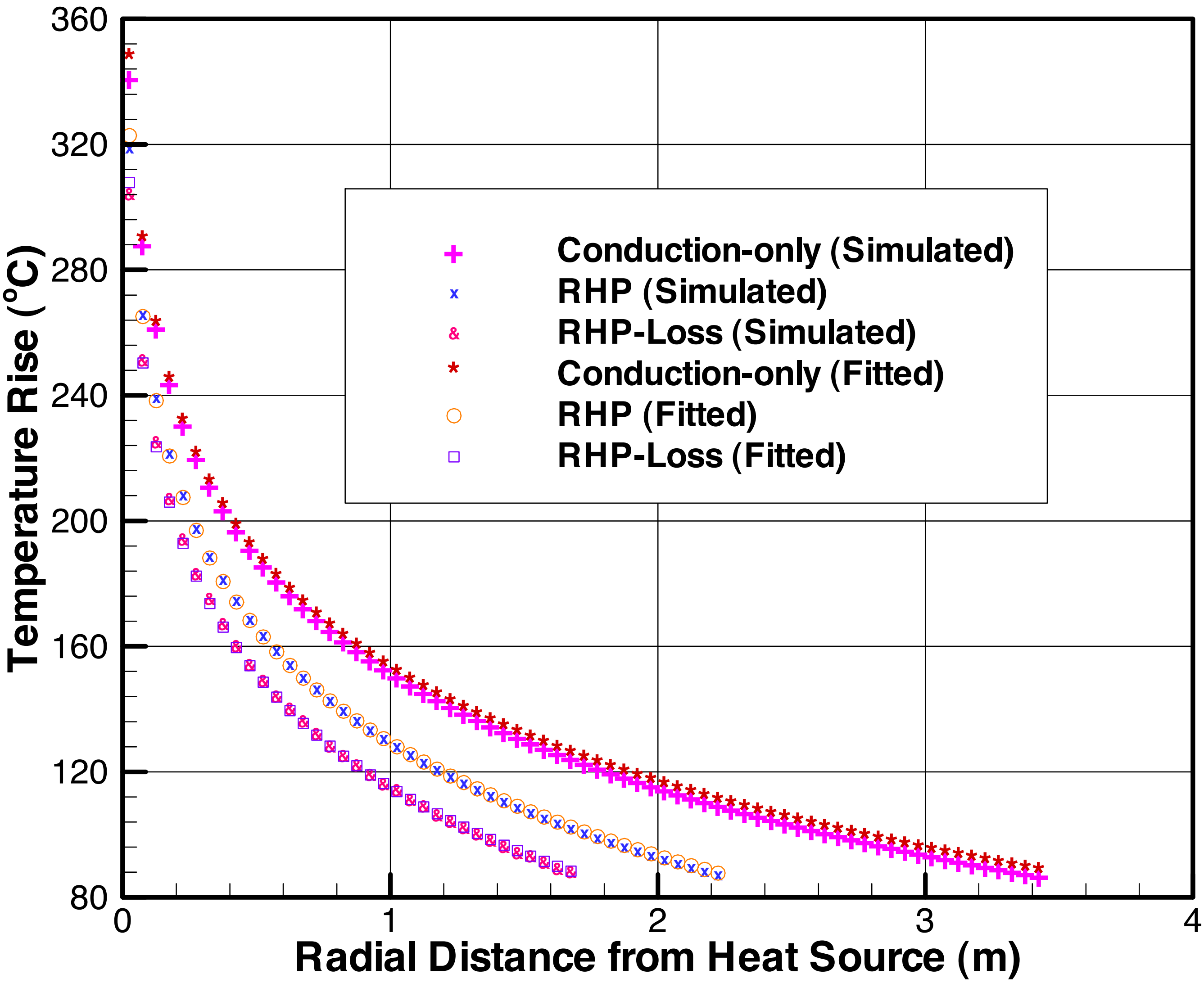

Conduction-only (Simulated)
RHP (Simulated)
RHP-Loss (Simulated)
Conduction-only (Fitted)
RHP (Fitted)
RHP-Loss (Fitted)
Temperature Rise (°C)
Radial Distance from Heat Source (m)
360
320
280
240
200
160
120
80
0
1
2
3
4

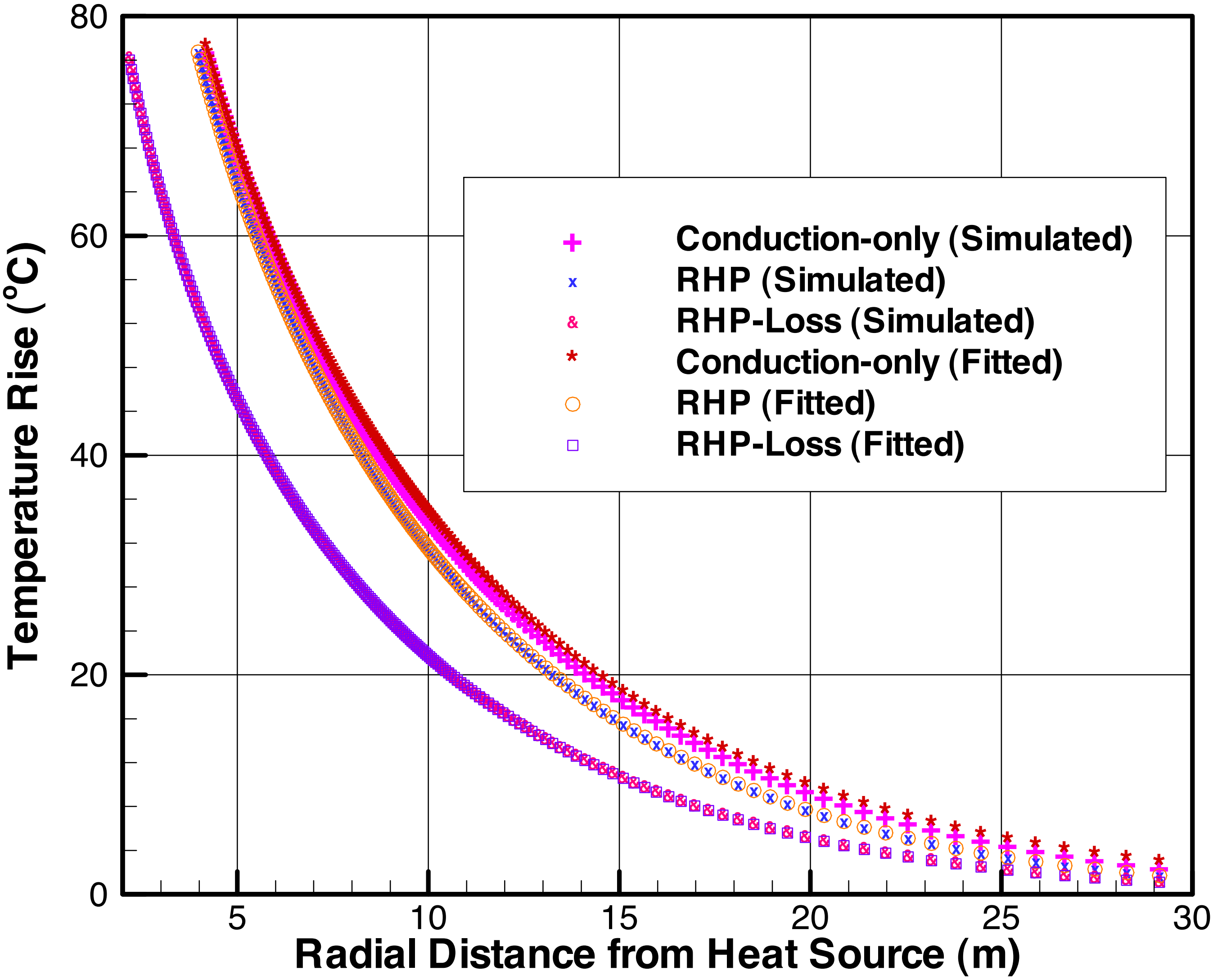

Temperature Rise (°C)
Radial Distance from Heat Source (m)
0
20
40
60
80
5
10
15
20
25
30
Conduction-only (Simulated)
RHP (Simulated)
RHP-Loss (Simulated)
Conduction-only (Fitted)
RHP (Fitted)
RHP-Loss (Fitted)

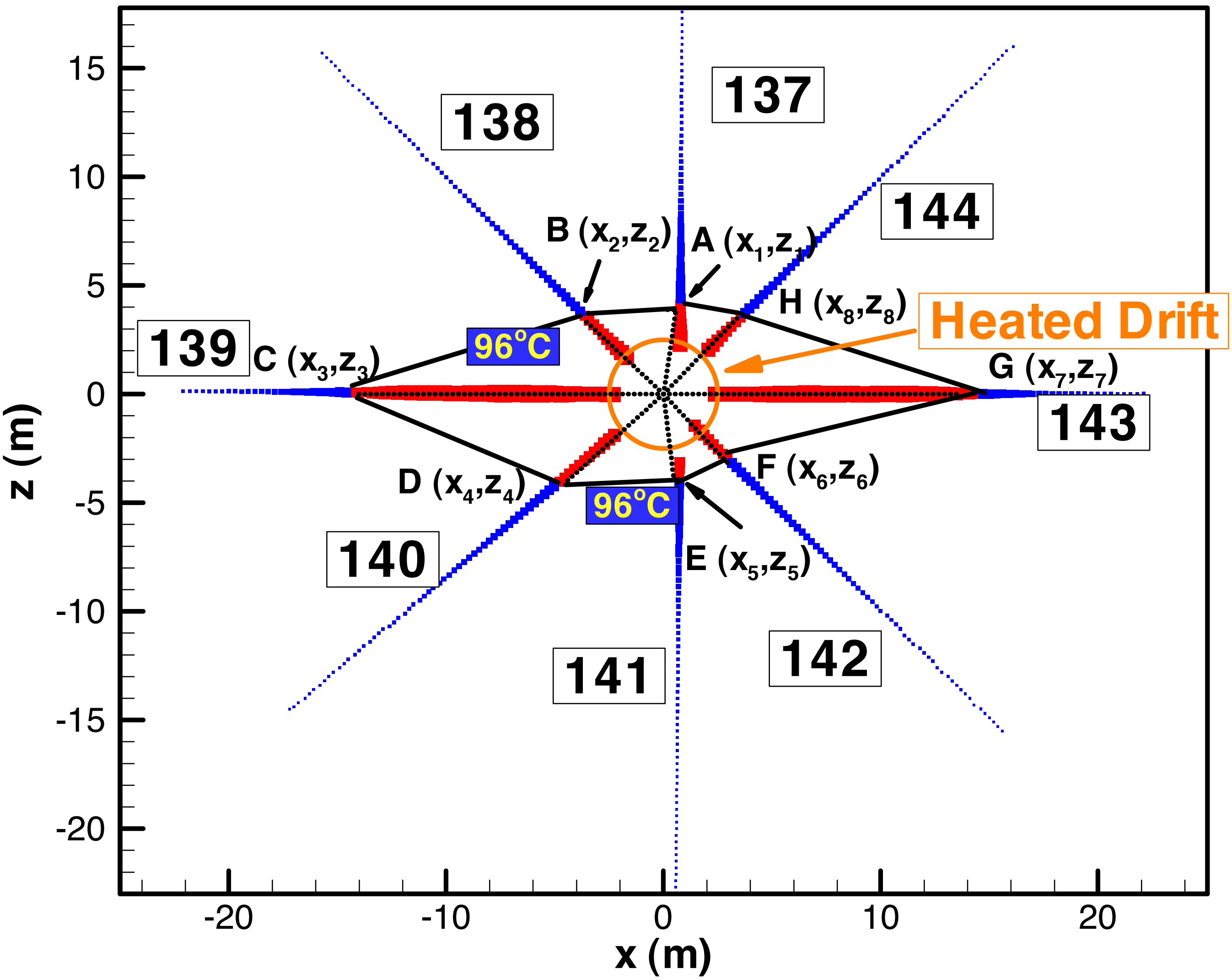

137
138
144
139
143
140
141
142
B (x2,z2)
A (x1,z1)
H (x8,z8)
C (x3,z3)
G (x7,z7)
D (x4,z4)
F (x6,z6)
E (x5,z5)
96°C
96°C
Heated Drift
x (m)
z (m)

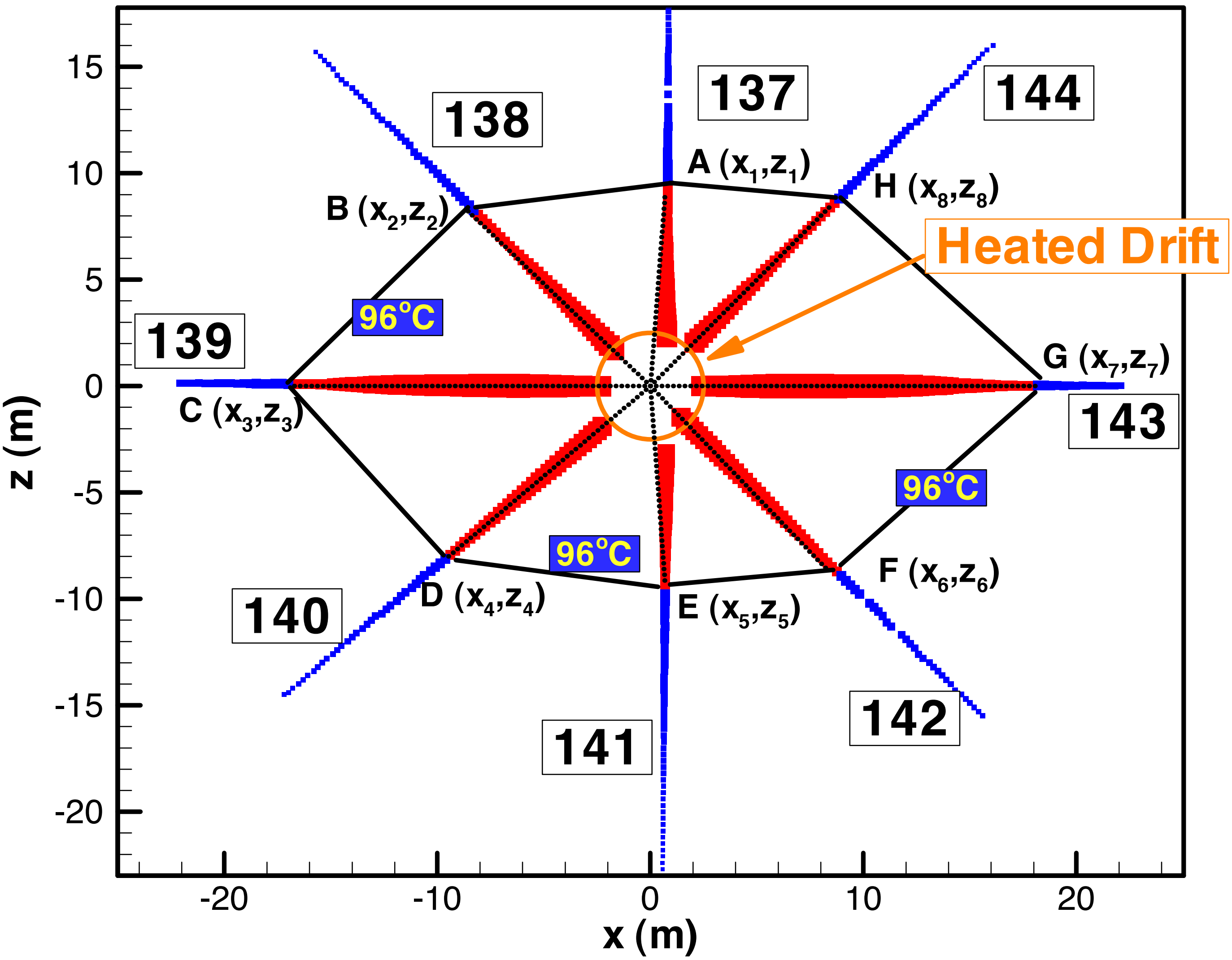

137
138
144
139
143
140
141
142
A (x1,z1)
B (x2,z2)
C (x3,z3)
D (x4,z4)
E (x5,z5)
F (x6,z6)
G (x7,z7)
H (x8,z8)
Heated Drift
96°C
96°C
96°C
z (m)
x (m)

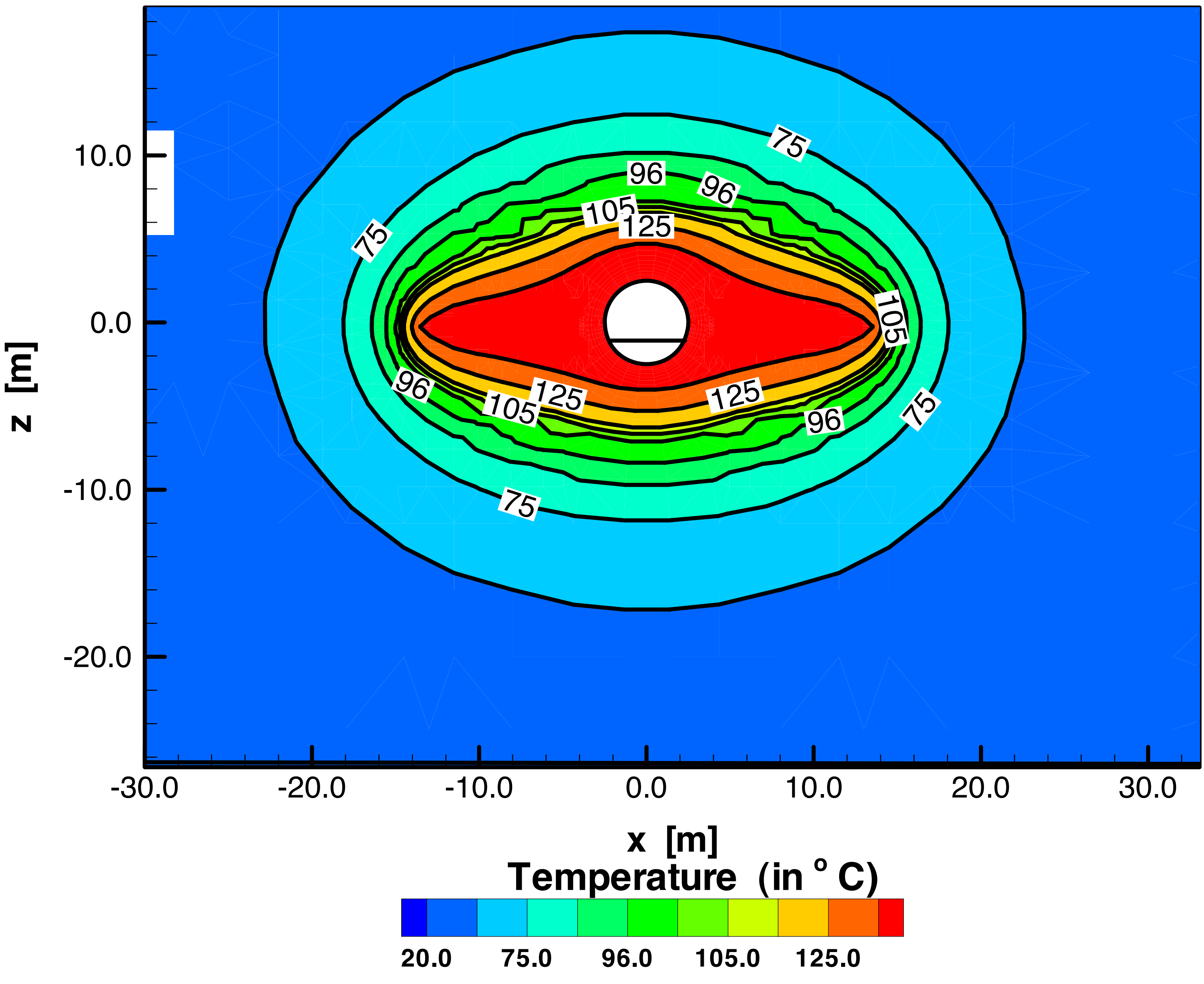
75
96
96
105
125
75
105
96
125
105
125
96
75
75
10.0
0.0
-10.0
-20.0
z [m]
-30.0
-20.0
-10.0
0.0
10.0
20.0
30.0
x [m]
Temperature (in ° C)
20.0
75.0
96.0
105.0
125.0

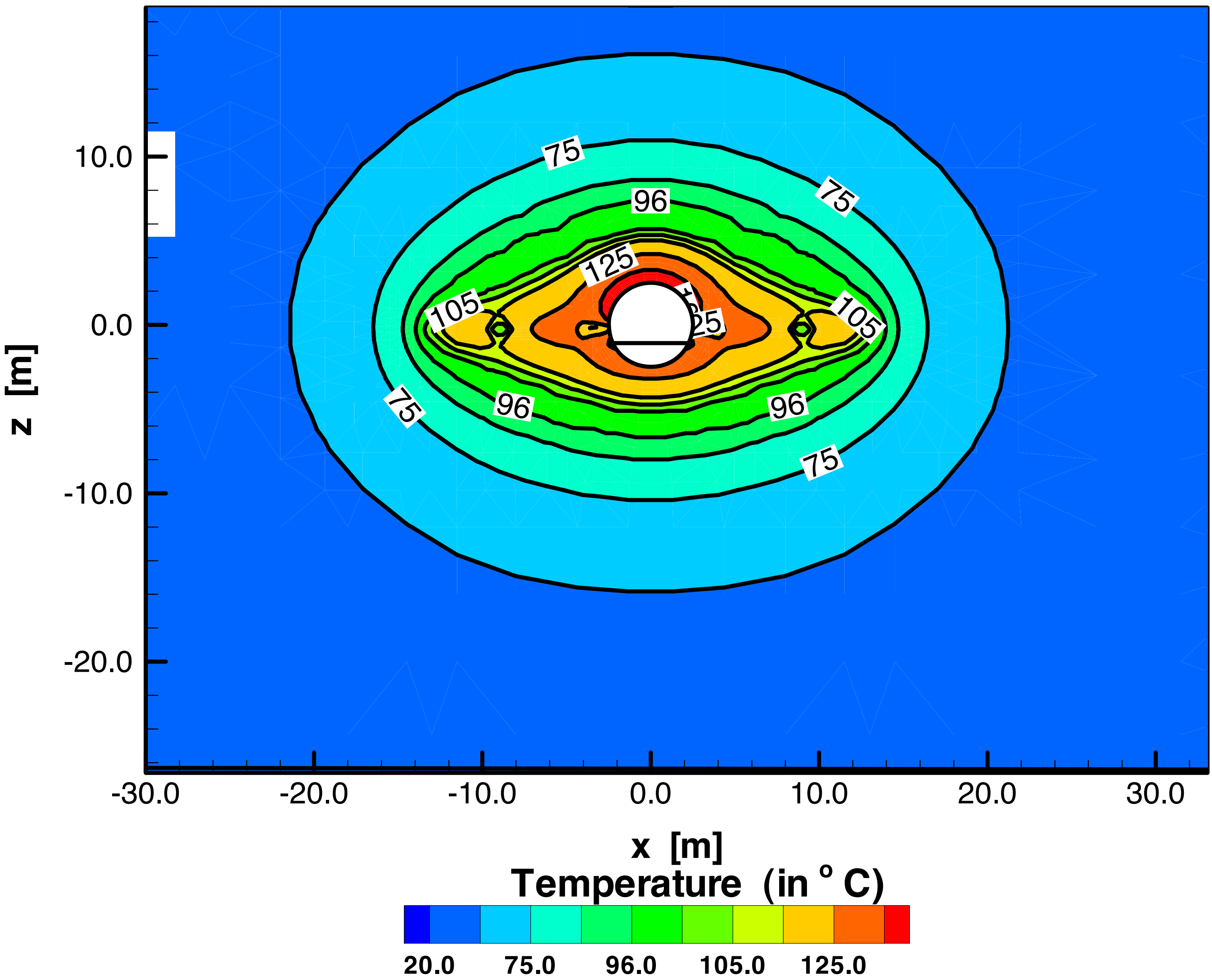

z [m]
x [m]
10.0
0.0
-10.0
-20.0
-30.0
-20.0
-10.0
0.0
10.0
20.0
30.0
75
96
105
125
Temperature (in ° C)
20.0
75.0
96.0
105.0
125.0

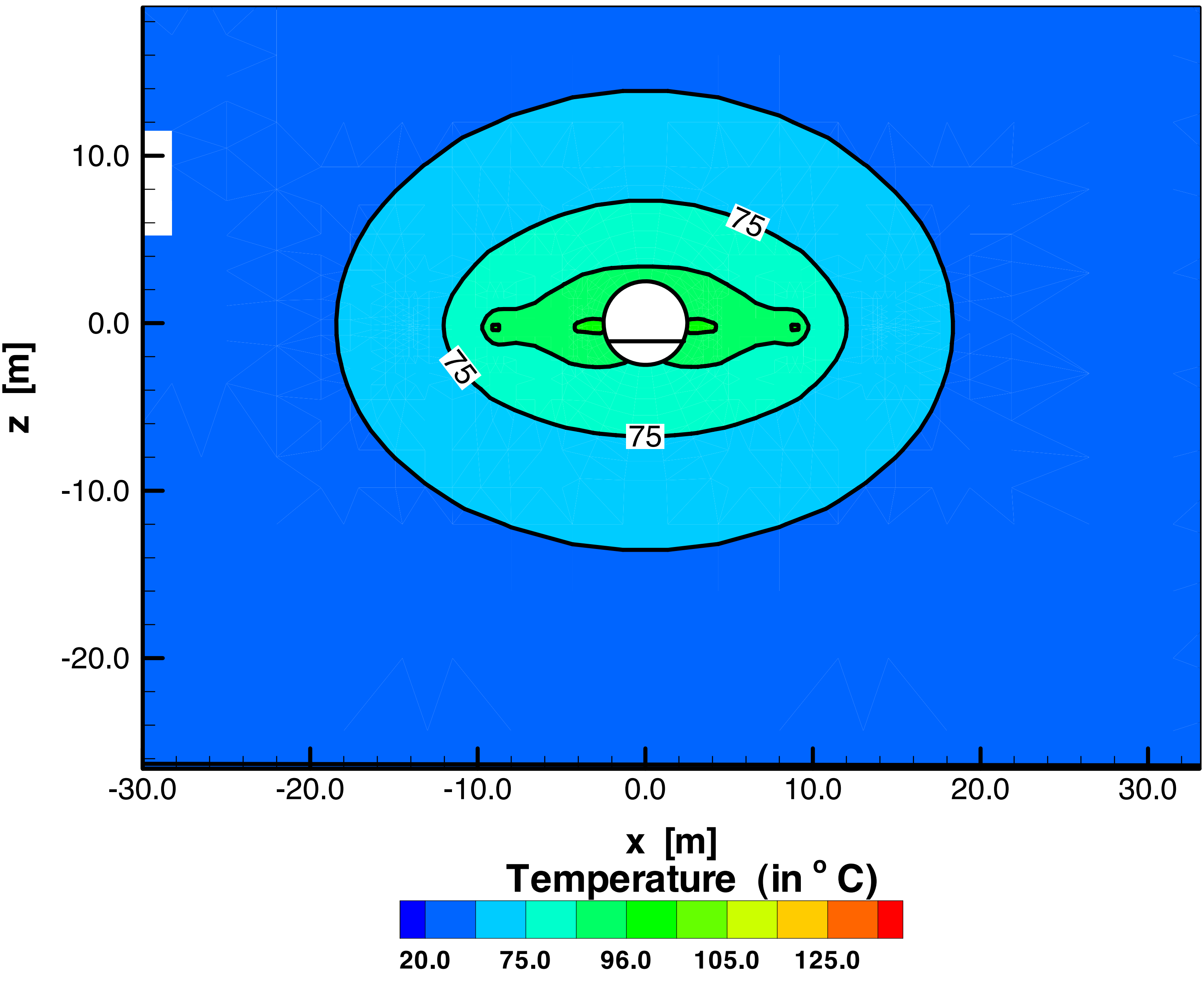
75
75
75
10.0
0.0
-10.0
-20.0
z [m]
-30.0
-20.0
-10.0
0.0
10.0
20.0
30.0
x [m]
Temperature (in ° C)
20.0
75.0
96.0
105.0
125.0

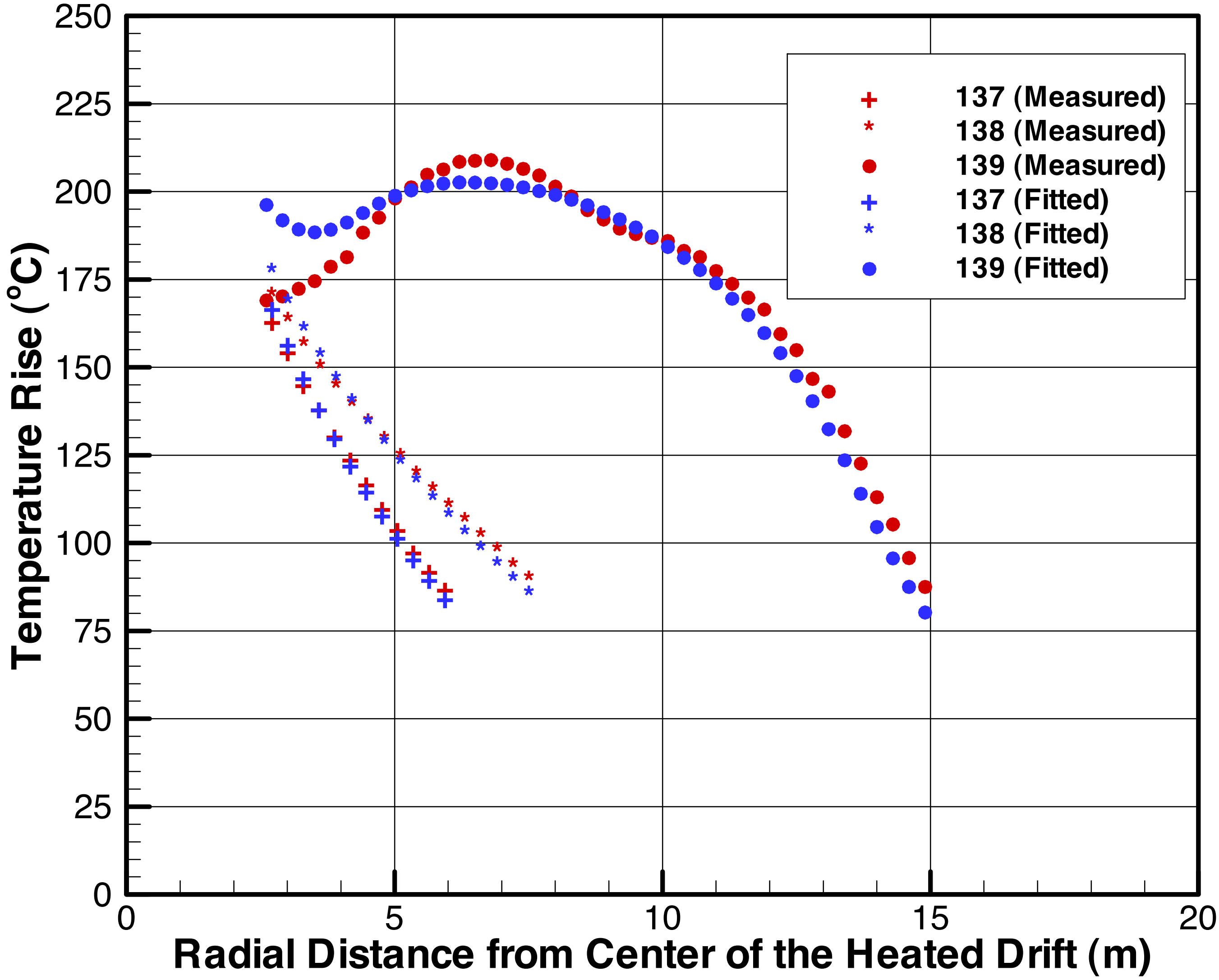

137 (Measured)
138 (Measured)
139 (Measured)
137 (Fitted)
138 (Fitted)
139 (Fitted)
Temperature Rise (°C)
0
25
50
75
100
125
150
175
200
225
250
Radial Distance from Center of the Heated Drift (m)
0
5
10
15
20

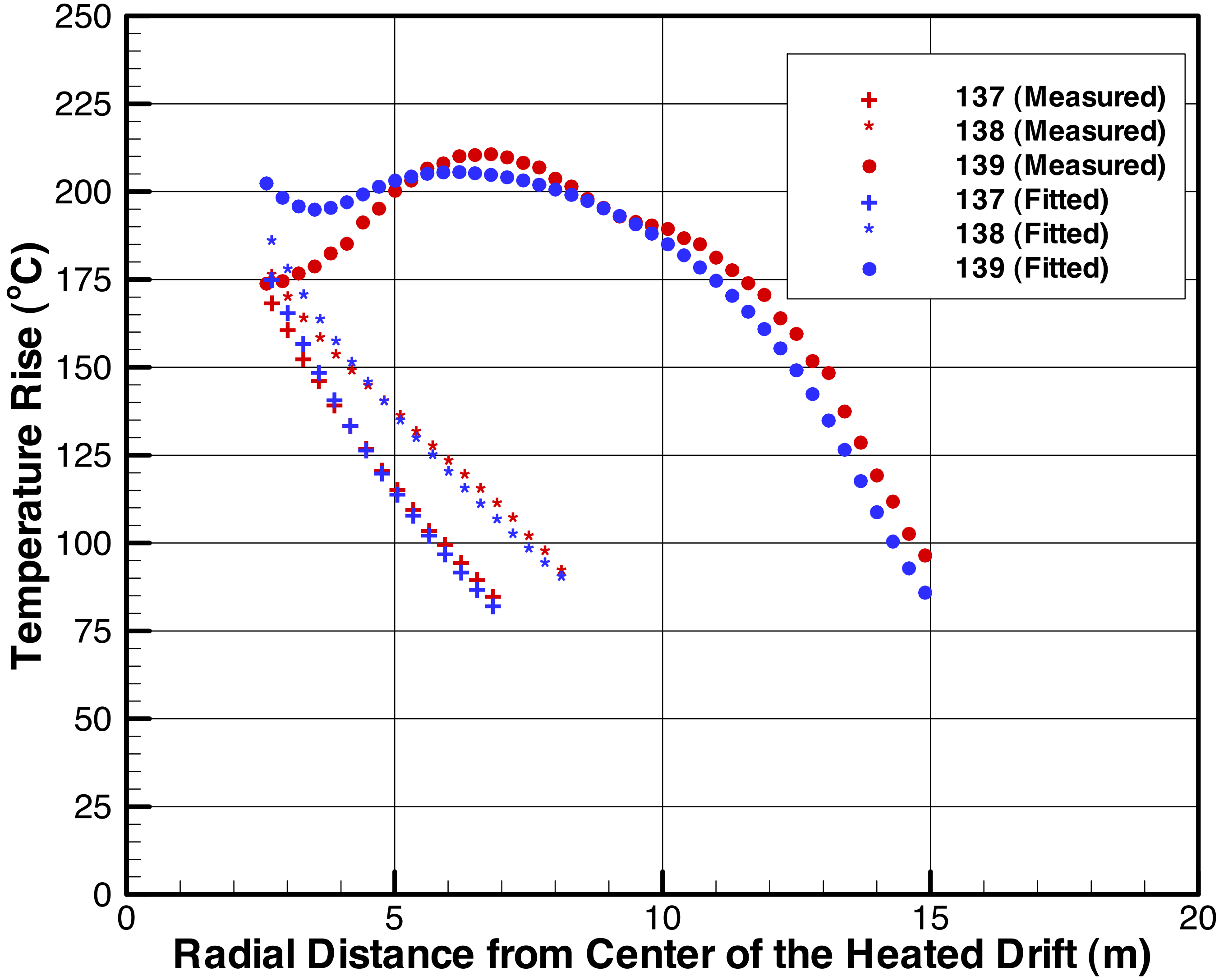

Temperature Rise (°C)
Radial Distance from Center of the Heated Drift (m)
0
25
50
75
100
125
150
175
200
225
250
0
5
10
15
20
137 (Measured)
138 (Measured)
139 (Measured)
137 (Fitted)
138 (Fitted)
139 (Fitted)

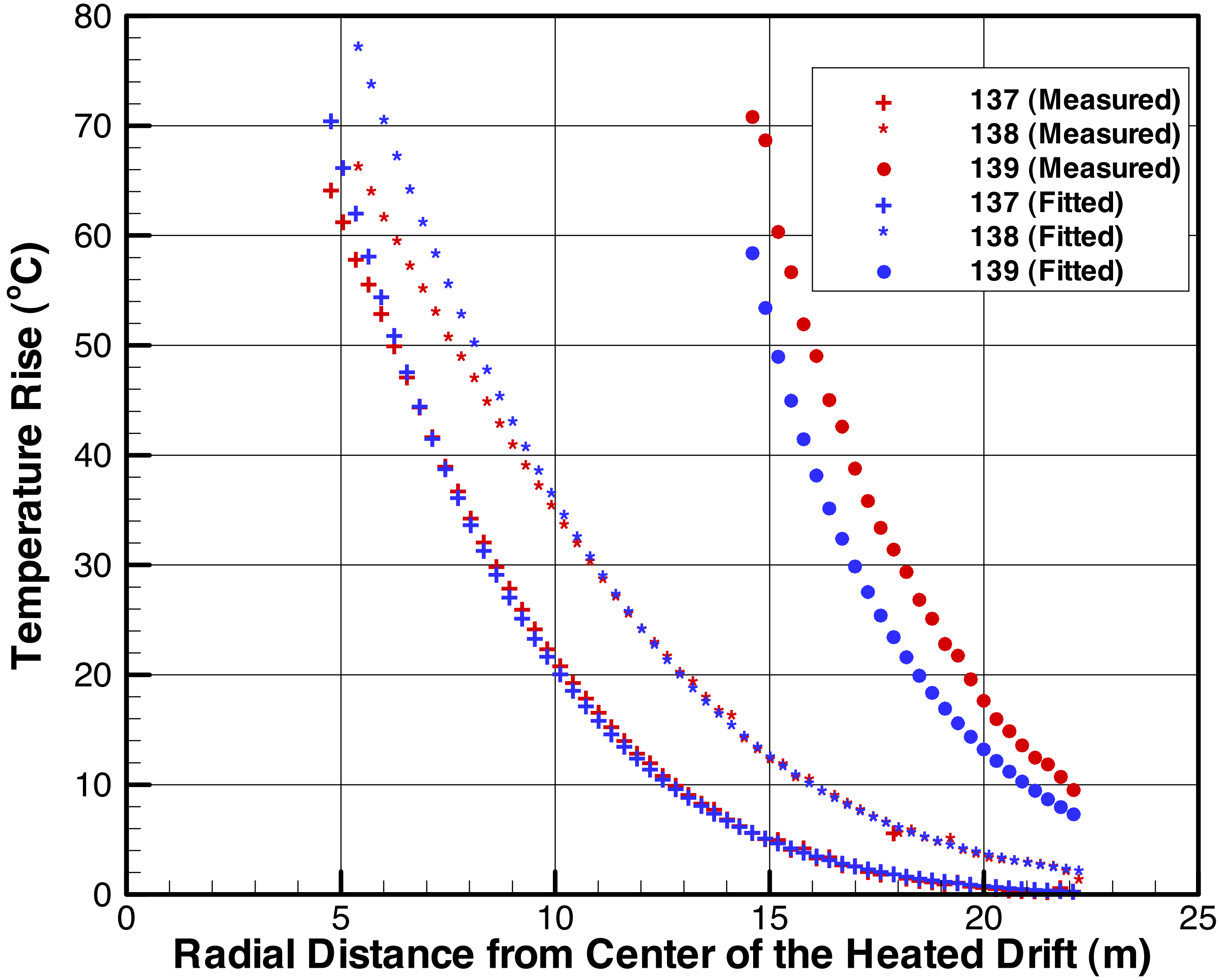

137 (Measured)
138 (Measured)
139 (Measured)
137 (Fitted)
138 (Fitted)
139 (Fitted)
Temperature Rise (°C)
Radial Distance from Center of the Heated Drift (m)
0
5
10
15
20
25
0
10
20
30
40
50
60
70
80

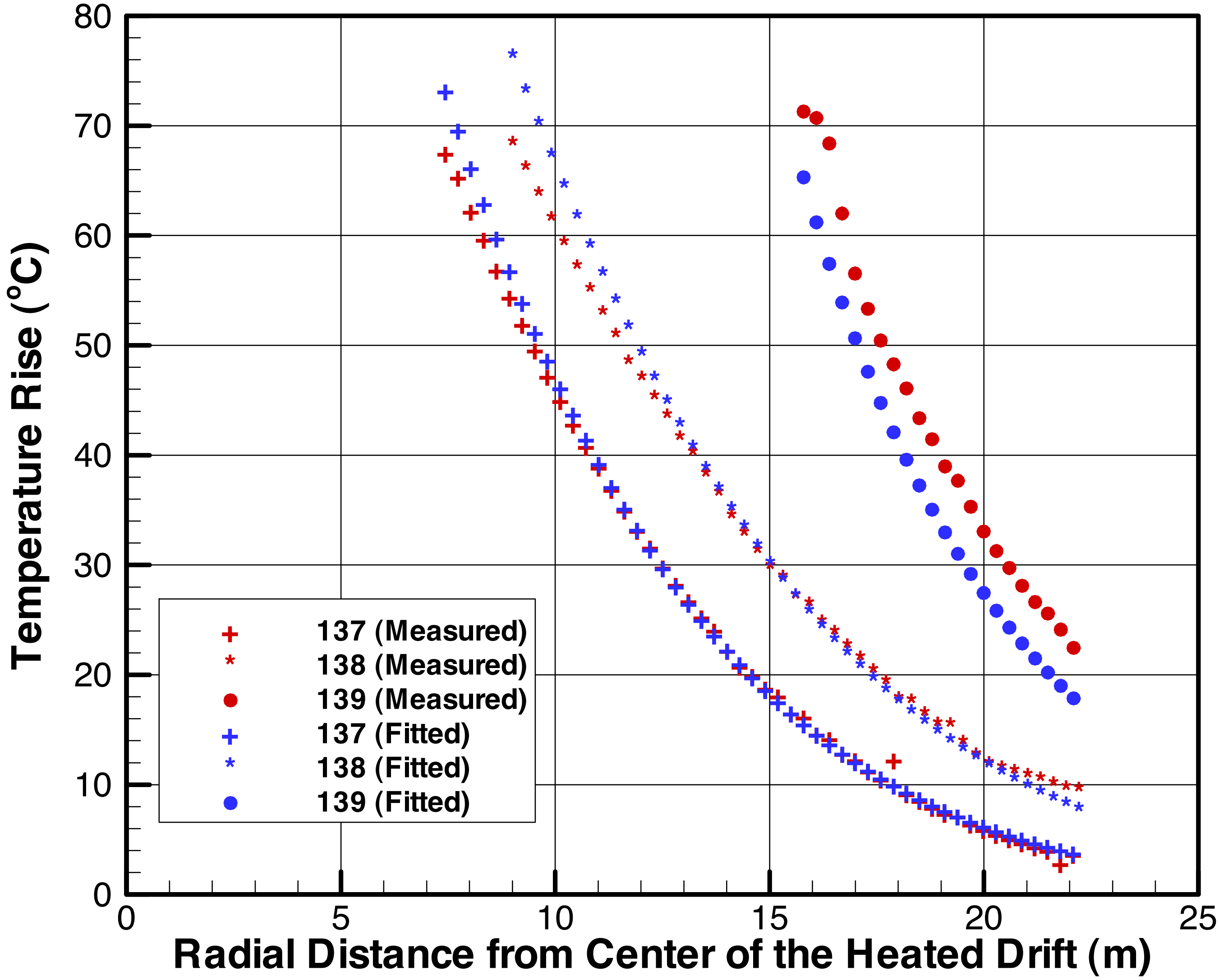

Temperature Rise (°C)
Radial Distance from Center of the Heated Drift (m)
137 (Measured)
138 (Measured)
139 (Measured)
137 (Fitted)
138 (Fitted)
139 (Fitted)
0
5
10
15
20
25
30
40
50
60
70
80